Melt Inclusions in Zircon: A Window to Understanding the Structure and Evolution of the magmatic system beneath the Laguna del Maule Volcanic Field

Kei Shimizu[a*], Tyler B. Blum[a], Chloe E. Bonamici[a], John H. Fournelle[a], Christine, E. Jilly-Rehak[b], Noriko T. Kita[a], Kouki Kitajima[a], Jacob D. Klug[a], Will O. Nachlas[a], Brad S. Singer[a], Michael J. Spicuzza[a], Alexander V. Sobolev[c], Bryan A. Wathen[a], John W. Valley[a]

[a]Department of Geoscience, University of Wisconsin-Madison, Madison, WI, USA

[c]Department of Earth and Planetary Sciences, Stanford University, Stanford, CA, USA

[d]University Grenoble Alpes, ISTerre, Grenoble, France

[*]Corresponding author at: Jacobs, NASA Johnson Space Center, 2101 NASA Parkway, MailCode XI3, Houston, TX 77058, United States. E-mail address: kei.shimizu@nasa.gov (K. Shimizu)

Abstract

Explosive silicic eruptions pose a significant threat to society, yet the development and destabilization of the underlying silicic magmatic systems are still controversial. Zircons provide simultaneous information on the trace element composition and age of silicic magmatic systems, while melt inclusions in quartz and plagioclase yield important constraints on their volatile content as well as storage depth. Melt inclusions in zircons (MIZs) combine these data from a single mineral grain, recording the age, storage depth, temperature, and composition of magmas, and thus provide unique constraints on the structure and evolution of silicic magmatic systems. We studied MIZs from the Laguna del Maule (LdM) volcanic field in the southern Andes that is among the most active Pleistocene-Holocene rhyolitic volcanic centers worldwide and a potentially hazardous system displaying inflation rates in excess of 25 cm/yr. The host zircon ages suggest that the LdM MIZ record extends to ~30 kyr before eruption, in contrast to the melt inclusions in LdM plagioclase and quartz crystals that formed only decades to centuries before

29 eruption. The major element compositions of MIZs are minimally affected by post-entrapment

30 crystallization, and agree well with the LdM rhyolitic whole rock data. The more evolved major

31 element composition of rle MIZs than rdm MIZs, suggests a long-term deeper connection of the

32 rdm crystal mush to a more primitive magma body than that of the rle. The evidence of slow H

33 diffusion observed in MIZs suggest that their H_2O contents are not significantly affected by

34 diffusion of H through the host zircon. The storage depths of 1.1 to 2.8 kbars recorded by the H_2O

35 contents of rdm and rle MIZs are consistent with the optimal emplacement window (2.0 ± 0.5

36 kbar) of silicic magma reservoir growth, storage, and eruptibility based on thermomechanical

37 modeling (Huber et al. 2019).

1. Introduction

Silicic magmatic systems can generate explosive eruptions of moderate to large sizes (<1 to >10^3 km^3), posing significant risks to local communities and potentially causing substantial disruptions to global climate patterns that can adversely affect human societies and natural ecosystems. Shallow silicic magmas are thought to reside in the crust in the form of a crystal mush comprising less than 50% of melt, making it too viscous to erupt in bulk (Hildreth 2004). The process by which magma reservoirs develop and expand to significant sizes in the shallow crust over thousands of years, as well as the factors that cause destabilization, unrest, and eruption, is a topic of debate (Mahood 1990; Bachmann and Bergantz 2004; Bindeman and Simakin 2014; Wolff et al. 2015). The emerging model of trans-crustal magmatic systems suggests that sub-volcanic magma storage and differentiation occurs within multiple mushy magma reservoirs distributed vertically throughout the crust (Cashman et al. 2017).

Zircons have the unique ability to provide simultaneous information on the trace element composition and age within a single crystal domain by in situ microanalytical techniques (e.g., Claiborne et al. 2010; Reid et al. 2011). The examination of zircon ages and compositions in silicic systems has revealed a variety of processes, such as long-term magma accumulation (10^3–10^4 years), the merging of magmas with differing compositions, and the remobilization of near-solidus silicic magma (e.g., Bindeman et al. 2008; Wilson and Charlier 2009; Charlier and Wilson 2010; Barker et al. 2014; Chamberlain et al. 2014; Wotzlaw et al. 2015; Reid and Vazquez 2017). Zircons have also provided constraints on the duration of mobile and eruptible magma storage prior to eruption, although conflicting observations have been made based on trace element diffusion profiles in zircon that suggest eruptible magmas are a transient feature in a predominantly cool, crystalline, and largely subsolidus crystal mush (Cooper and Kent 2014; Rubin et al. 2017; Szymanowski et al. 2017), while Ti-in-zircon temperatures suggest storage of eruptible magma for a 10^3–10^4 year time scale (Barboni et al. 2016).

Eruptible rhyolite can be extracted via gravitational compaction and hindered settling (Bachmann and Bergantz 2004), while injections of hotter primitive magma catalyze this process by thermally rejuvenating the crystal-rich magma or remelting the silicic crust and cumulate (Mahood 1990; Bachmann and Bergantz 2004; Bindeman and Simakin 2014; Wolff et al. 2015).

67   Volatiles such as CO_2 and H_2O play an important role, as they can transfer heat from a degassing

68   primitive magma to the overlying crystal mush (e.g., Bachmann and Bergantz 2006), promote

69   melt migration through a crystal mush (e.g., Huber and Parmigiani 2018), cause second boiling,

70   inflation of magma reservoir, and explosive behavior (Blundy and Cashman 2008). Melt inclusions

71   in minerals such as quartz and plagioclase provide important constraints on the volatile content

72   of the primitive and more evolved magma, as well as their storage depth (Wallace et al. 1999;

73   Blundy and Cashman 2005; Wallace 2005).

74   We present major element and H_2O contents of melt inclusions in zircon (MIZs) and the

75   trace element composition and ^{230}Th-^{238}U ages of the host zircons erupted in the rhyolitic LdM

76   volcanic field. Values of δ^{18}O are also reported for MIZs and host zircons. LdM volcanic field is

77   among the most active Pleistocene-Holocene rhyolitic volcanic centers worldwide and a

78   potentially hazardous system showing inflation rates >25 cm/yr (Singer et al. 2014a). MIZs can

79   record volatile saturation pressure (H_2O-CO_2 in MIZ), temperature (Ti-in-zircon thermometer),

80   composition (MIZ major and trace element), and time (^{230}Th-^{238}U ages) that provide a unique set

81   of constraints on the understanding of the structure and evolution of silicic magmatic systems

82   (e.g., Thomas et al. 2003). Using our data, we distinguish and evaluate the effect of post-

83   entrapment modification versus primary magmatic processes on the MIZ composition through

84   crystallization and diffusive exchange. We then use our data to examine the structure and storage

85   conditions of magma reservoirs at LdM through time.

86

87   2. Geological setting

88   The Laguna del Maule volcanic field is located in the Southern Volcanic Zone (SVZ) of

89   central Chile, 30 km behind the active volcanic front (Fig. 1). The volcanism at LdM has been

90   dominantly silicic and concentrated within the central lake basin since the most recent glacial

91   retreat, which is estimated to have occurred locally at c. 23 to 19 ka based on ^{40}Ar/^{39}Ar dates of

92   unglaciated lava flows (Singer et al. 2000; Andersen et al. 2017). Both effusive and explosive

93   eruptions at LdM yielded rhyolites that contain less than 10 vol.% phenocrysts of plagioclase,

94   biotite, and magnetite ±quartz ±amphibole ±zircon. The 20 km^3 plinian Rhyolite of Laguna del

95   Maule (rdm), thought to have erupted from a vent beneath the modern lake (Fierstein 2018), is

96   the earliest known post-glacial rhyolite. The subsequent rhyolite eruptions, each less than 3 km^3

97   in volume, occurred most frequently during an early post-glacial (EPG) period from 22.5 to 19 ka,

98   and during the middle to late Holocene. Rhyodacite and andesite eruptions also occurred

99   throughout post-glacial times, but comprise a smaller cumulative volume than the rhyolites and

100   were concentrated in the western LdM basin, away from the locus of rhyolite volcanism. Based

101   on these observed spatial relations, Hildreth et al. (2010) proposed that a massive silicic magma

102   reservoir is present below LdM, obstructing the rise of mafic magma.

103   This hypothesis is increasingly supported by geological, geochronological, and geophysical

104   studies, which suggest that the shallow magma system is still active at present with ongoing

105   average inflation of ~20 cm/year since 2007 (up to 29 cm/year) (Feigl et al. 2014; Le Mevel et al.

106   2015; Le Mevel et al. 2016; Andersen et al. 2017; Miller et al. 2017; Andersen et al. 2018; Cordell

107   et al. 2018; Fierstein 2018; Singer et al. 2018; Wespestad et al. 2019; Le Mével et al. 2021). Both

108   surface- and teleseismic-tomography have shown the presence of a crystal-rich reservoir with

109   450 to 500 km^3 of partial melt at a depth of 2-12 km beneath the northwest portion of the lake

110   at LdM (Wespestad et al. 2019; Bai et al. 2020). Magnetotelluric observation suggests the

111   presence of a deeper partially molten reservoir that extends beyond 15 km depth (Cordell et al.

112   2018; Cordell et al. 2019).

113   Plagioclase trace element compositions as well as plagioclase and quartz melt inclusions

114   have provided constraints on magma extraction processes and magma storage conditions that

115   have not been available from whole rock data (Andersen et al. 2018; Klug et al. 2020). Trace

116   element diffusion modeling of LdM plagioclase suggests a short time scale (decades to centuries)

117   between extraction of crystal-poor rhyolite from crystal mush and its eruption (Andersen et al.

118   2018). Melt inclusions in plagioclase and quartz revealed shallowing storage depth with

119   increasing degree of melt differentiation, with the latter being more evolved and recording lower

120   H_2O contents/shallower storage depth (Klug et al. 2020). Based on these observations, Klug et al.

121   (2020) argued that crystal-poor rhyolite went through decompression-driven fractional

122   crystallization as it ascended from ~14 km to ~4 km shortly before eruption (Klug et al. 2020).

123   Zircon petrochronology records up to 160 kyr of rhyolitic magma production in the crystal

124   mush reservoir of the LdM (Andersen et al. 2019). The significant age difference between

125 plagioclase and quartz (decades to centuries) compared to zircon has been attributed to

126 extraction of rhyolite from a crystal mush entraining smaller zircons preferentially over larger

127 crystals of major phases (Claiborne et al. 2010; Stelten and Cooper 2012; Andersen et al. 2019).

128 Based on the Ti-in-zircon thermometry as well as modeling of zircon crystallization rates,

129 contemporaneous existence of hot zones and regions of cold storage within the mush reservoir

130 has been hypothesized (Andersen et al. 2019).

131

132 ## 3. Samples and Methods

133 ### 3.1 Samples

134   The sample that is the main focus of this study is from the 20 km^3 plinian rdm unit (22.5

135 to 19 ka) that comprises ash and pumice lapilli (up to 4 cm in diameter) from quickly cooled

136 tephra within well-defined stratigraphic sections (Klug et al. 2020). We report data from an

137 additional sample of the Los Espejos rhyolite (rle) unit, which erupted at 19.0 ± 0.4 ka subsequent

138 to rdm (Andersen et al. 2017).

139

140 ### 3.2 Mount preparation

141   A ~2 kg pumice sample of the rdm unit was crushed and sieved into ≥ 250 μm and < 250

142 μm size fractions. Approximately 1000 zircon grains were separated from the < 250 μm fraction

143 using conventional techniques including Wilfley-type shaking table, Frantz isodynamic magnetic

144 separator, and heavy liquid separation. The zircon grains were then handpicked, cast in epoxy

145 grain mounts, and polished. At least two grains each of UWZ-1 zircon (WiscSIMS, unpublished)

146 and UWQ-1 quartz (Kelly et al. 2007) standards were also cast in the same mount. The relief

147 between the grains and adjacent epoxy was minimized to < 1 μm and grains were placed in the

148 central 80 mm radius region of the mount to ensure good spot-to-spot reproducibility (Kita et al.

149 2009; Peres et al. 2013). In addition to the epoxy mount, we also studied a mount with LdM

150 zircons that was prepared and analyzed by Andersen et al. (2019) who pressed the zircon grains

151 into soft indium and analyzed euhedral crystal faces for trace elements and ^{230}Th-^{238}U isotope

152 ratios. The indium mount was then polished to expose the crystal interiors which were also

153 analyzed for trace elements and ^{230}Th-^{238}U isotope ratios by Andersen et al. (2019). The MIZs

154 exposed in these zircons were studied here, which are all from the rle unit.

155

3.3 Imaging of zircons/MIZs

157 Zircons were imaged by reflected light, backscattered electrons (BSE), and

158 cathodoluminescence (CL) using a Hitachi S-3400N Scanning Electron Microscope (SEM) and

159 Gatan Chroma CL system at the University of Wisconsin–Madison. For both the epoxy and indium

160 mounts, we focused only on zircons that have MIZs. The crystal sizes range from 57 to 174 µm

161 on the long axis and 26 to 88 µm on the short axis with aspect ratios of 1 to 3.3 (Figs. 2 and S1).

162 Zircon morphologies range from anhedral to euhedral and prismatic and are the crystals are clear

163 and colorless. In CL, the zircons are characterized by sector and oscillatory zoning. Around some

164 melt/mineral inclusions, the host zircon is characterized by undulating CL pattern and/or bright

165 CL (Fig. S1).

166 All zircon grains were imaged by BSE to look for MIZs exposed at the grain surface. A

167 potential issue to this approach is that some of the 3D context of the MIZ and host zircon is lost

168 from the polishing process of exposing the MIZ. This limits certain characterization of the MIZs

169 such as their volume and dimensions, their spatial distribution within the host zircon, as well as

170 the potential presence of vapor bubbles and crystals (e.g., Sobolev and Kostyuk 1975; Roedder

171 1984; Bodnar and Student 2006; Rose-Koga et al. 2021) in the MIZs that may have been polished

172 away. Despite the loss of certain 3D context, it is highly unlikely that the MIZs were

173 embayment/melt channel that were in contact with the surrounding melt based on the clearly

174 distinct H_2O content and major element composition of the MIZs compared to those of the

175 surrounding melt (i.e., matrix glass) (sections 4.2 and 4.3) indicating lack of communication

176 between the MIZs and the surrounding melt.

177 Qualitative analyses of major elements of MIZs were done by an Oxford AZtecOne energy-

178 dispersive X-ray spectroscopy (EDS) system with acceleration voltage and beam current of 15 kV

179 and 1 nA, respectively. We carefully selected MIZs that are glassy and homogeneous. We also

180 avoided MIZs that are visibly intersected by cracks in the host zircon. The nineteen MIZs identified

181 in 17 rdm zircon grains range from 8 to 25 µm on the long axis and 5 to 14 µm on the short axis

182　with aspect ratios of 1.1 to 5.3 (Figs. 2 and S1). Six MIZs found in the rle zircons range from 5 to

183　43 μm on the long axis and 3 to 5 μm on the short axis with aspect ratios of 1.1 to 8.7 (Figs. 2 and

184　S1). On the exposed surface, all 25 MIZs are glassy and 20 are completely homogeneous while 5

185　of them are mostly homogeneous except small microcrystals of titanomagnetite and pyroxene

186　(not shown). Nineteen of the MIZs are circular to oval in shape, while six are elongated to

187　irregularly shaped. Four out of 17 zircons have matrix glass adhered onto them.

188

189　**3.4 EPMA of MIZs**

190　　　　Chemical composition of the MIZs was measured with a CAMECA SXFive Field Emission

191　Electron Probe Microanalyzer (FE-EPMA) at the Department of Geoscience at the University of

192　Wisconsin–Madison. The epoxy mount was coated with a 20 nm carbon layer after being cleaned

193　with distilled water and ethanol. Analyses were conducted with an accelerating voltage of 15 kV,

194　a beam current of 1 nA, and a beam diameter of 2 or 3 μm. The low beam current was selected

195　to minimize beam induced element migration during the EPMA measurements. Major elements

196　(Na, Al, Si, Mg, K, Ca) were measured for 200 s and quantified using Mean Atomic Number (MAN)

197　background regression (Donovan et al. 2016). Oxygen and the remaining minor elements (P, Fe,

198　Mn, Ti, Zr) were quantified using off-peak background regression and measured for 60 s on peak

199　and 30 s on each high and low background position. An exponential background regression was

200　used for analysis of O. Time-dependent intensity corrections were applied for Na, K, Si, and O.

201　Analysis of hydrous haplogranite glass (6.6 wt% H_2O; Morgan and London 2005) was used to

202　evaluate accuracy of the analytical routine. Many of the zircon MIZs had diameter < 5 μm. This

203　resulted in secondary fluorescence of Zr from the surrounding zircon matrix. Monte-Carlo

204　simulation of electron-specimen interactions using PENEPMA was used to constrain the extent

205　of secondary fluorescence for various inclusion dimensions and beam diameters. Addition of Zr

206　into the analysis routine was used to monitor the effects of secondary fluorescence on individual

207　measurements; any measurements with >1 wt% ZrO2 were interpreted as affected by secondary

208　fluorescence and discarded from consideration. For MIZ analyses with < 1 wt.% ZrO_2, the

209　compositions were corrected to be ZrO_2-free, assuming essentially all Zr signal was from host

210　zircon.

211

3.5 SIMS

3.5.1 Zircon $\delta^{18}O$; MIZ $\delta^{18}O$ and H_2O

Zircon oxygen isotope ratios as well as MIZ oxygen isotope ratios and H_2O contents were measured using the CAMECA IMS-1280 secondary ion mass spectrometer (SIMS) at the WiscSIMS laboratory at the University of Wisconsin–Madison. The zircon epoxy mount was gold-coated after being cleaned with distilled water and ethanol and kept in a vacuum oven at 60ºC for 24 hours. Zircon analyses were made following the methods described previously (Kita et al. 2009; Valley and Kita 2009; Wang et al. 2014), with a primary $^{133}Cs^+$ ion beam was focused to 10 µm diameter with an intensity of 1.7 to 1.8 nA, to generate ~3×10^9 counts per second (cps) of secondary $^{16}O^-$ ions. The multicollection (MC) Faraday cup (FC) detectors were used to simultaneously measure $^{16}O^-$, $^{18}O^-$, and $^{16}O^1H^-$ signals with feedback resistors of 10^{10}, 10^{11}, and 10^{11} Ω, respectively. Individual zircon analyses lasted approximately 3.5 min including sputtering of the gold coated surface (10 s), automatic centering of the secondary ion beam in the field aperture (60 s), and 40 cycles of 4 second integrations of oxygen ion measurements. Analysis pits were ~2 µm deep. For the MIZ analysis, the primary Cs^+ ion beam was focused to 3 µm diameter with an intensity of 25 pA, to generate ~3.5×10^7 counts per second (cps) of secondary $^{16}O^-$ ions. Each MIZ analyses lasted approximately 4 min including sputtering of the gold coated surface (30 s), automatic centering of the secondary ion beam in the field aperture (60 s), and 20 cycles of 8 second integrations of oxygen ion measurements. The $^{16}O^-$ and $^{18}O^-$, and $^{16}O^1H^-$ signals were measured simultaneously in two FCs ($^{16}O^-$ and $^{16}O^1H^-$, both with feedback resistors of 10^{11} Ω) and one electron-multiplier (EM) for $^{18}O^-$ (~7×10^4 cps). Hydride interferences at mass 18 were resolved at mass resolving power (MRP at 10% peak height) of 2,200, and MRP of 5,000 was used for mass 17 to resolve $^{16}O^1H^-$ from $^{17}O^-$. A liquid N_2 trap was used to maintain vacuum in the sample chamber ≤ 5×10^{-9} mbar to reduce hydrogen background. Four analyses of UWZ-1 zircon standard were made at the beginning of the session and after every 10 unknowns. The bracketing sets of eight analyses of UWZ-1 ($\delta^{18}O$ = 4.98 ‰ VSMOW) were used to monitor instrumental bias for zircon standard and the spot-to-spot reproducibility for individual brackets, which ranged

9

239 between 0.17 and 0.21 ‰ (2SD) for the zircon analyses and 0.51 to 0.75 ‰ (2SD) for the MIZ

240 analyses.

241 For H_2O contents of MIZs, calibration was made between the measured $^{16}O^1H^-/^{16}O^-$ and

242 H_2O content using rhyolitic glasses standards with known H_2O concentrations (Newman et al.

243 1986; Singer et al. 2014b; Klug et al. 2020). The major element compositions of these rhyolitic

244 glass standards encompass those observed in the MIZ (Fig. S2). For the February 2022 session,

245 we obtained a linear regression line between $^{16}O^1H^-/^{16}O^-$ versus H_2O wt.% (0.33 to 3.51 wt.% H_2O

246 rhyolitic glasses; Newman et al. (1986), Klug et al. (2020)) (Fig. S3a, Table S2). The majority of MIZ

247 H_2O contents obtained during this session were beyond the calibration range (> 3.5 wt.%). A

248 subsequent session in June 2022 was conducted, in which we measured higher H_2O content

249 standards (0 to 6.09 wt.% H_2O rhyolitic glasses; Singer et al. (2014b)). We obtained a polynomial

250 regression line between $^{16}O^1H^-/^{16}O^-$ versus H_2O wt.% (Fig. S3b, Tables S3). The H_2O contents of a

251 set of MIZs agree to within 10% on average between the February and June 2022 sessions (Fig.

252 S3c). For both sessions, the background levels of $^{16}O^1H^-/^{16}O^-$ were determined by multiple

253 analyses of the UWZ-1 zircon grains, which were subtracted from the $^{16}O^1H^-/^{16}O^-$ of the melt

254 inclusion analyses before converting them to H_2O wt.%. The background corrections were

255 typically smaller than 10% of measured $^{16}O^1H^-/^{16}O^-$ values. To correct for MIZ $\delta^{18}O$ instrumental

256 mass fractionation, anhydrous glass standards with known $\delta^{18}O$ (Jochum et al. 2006) were

257 analyzed that have a range of SiO_2 from 51.4 to 75.6 wt.% (Tables S2 and S3). The $\delta^{18}O$ bias was

258 estimated relative to zircon (bias*) as a function of the SiO_2 content of the glass standards. The

259 $\delta^{18}O$ of individual MIZs were corrected for the bias based on the bias estimated from bracketing

260 zircon standard analyses and the relative bias (bias*) of each MIZ that is calculated using the SiO_2

261 content (EPMA data). The effect of H_2O on the MIZ $\delta^{18}O$ instrumental mass fractionation was

262 evaluated using some of the aforementioned hydrous rhyolitic glass standards that were

263 previously analyzed for $\delta^{18}O$ (Newman et al. 1988; Eiler et al. 2000). This showed that the

264 instrumental biases of the hydrous glasses agree well with those of the anhydrous glasses such

265 that the effect of H_2O on the MIZ $\delta^{18}O$ instrumental mass fractionation is minimal.

266

267 **3.5.2 Zircon trace elements**

268   Zircons were analyzed for 26 trace elements (Al, P, Ca, Sc, Ti, Fe, Y, Nb, La, Ce, Pr, Nd, Sm,

269   Eu, Gd, Tb, Dy, Ho, Er, Tm, Yb, Lu, Hf, Ta, Th, U) using the CAMECA IMS-1280 secondary ion mass

270   spectrometer (SIMS) at the WiscSIMS laboratory at the University of Wisconsin–Madison.

271   Analyses used a $^{16}O^-$ primary beam at a current of 5.4 nA and a total impact energy of 23 kV (−13

272   kV at the ion source and +10 kV on the sample surface). Analytical pits were ~13 μm in diameter.

273   The mass spectrometer was operated at a nominal mass resolving power (MRP = M/ΔM) of

274   14,000, which allows for separation of $^{45}Sc^+$ and $^{93}Nb^+$ from interferences with $^{90}Zr^{++}$ and $^{92}ZrH^+$,

275   respectively (e.g., Grimes et al. 2015; Coble et al. 2018; Blum et al. 2023). No energy offset was

276   applied because most molecular interferences, such as REE oxides on REE, were fully resolved.

277   Each analysis included a 30 second pre-sputter, centering of the secondary beam within the field

278   aperture, and five cycles of counting from low to high mass by magnetic peak-jumping on axial

279   mono-collector (mostly EM except for major element Si and Zr peaks on FC). Normalized count

280   rates (normalizing species ^{28}Si) are converted to trace element concentrations based on element

281   specific relative sensitivity factors (RSFs). RSFs were determined for the primary reference

282   material, NIST610 (Pearce et al. 1997) with correction factors based on multiple zircon reference

283   materials to account for matrix mismatch between glass and zircon, similar to those in previous

284   studies (Page et al. 2007; Bouvier et al. 2012; Kitajima et al. 2012). Zircon reference materials

285   analyzed in this study are 91500 (Wiedenbeck et al. 2004; Coble et al. 2018), MAD-559 (Coble et

286   al. 2018), and GZ7 (Nasdala et al. 2018). For elements (Al, Ca, Sc, and Fe) that do not have

287   homogeneous or well characterized published values in the reference material suite, no

288   correction factor is applied (Wiedenbeck et al. 2004; Coble et al. 2018). Additional analytical

289   details will be published elsewhere.

290

291   **3.5.3 Zircon ^{230}Th-^{238}U**

292   To prepare the zircon epoxy grain mount for SIMS U-Th analyses, the mount was cleaned

293   with a 10% EDTA (ethylenediaminetetraacetic acid) wash, thoroughly rinsed with DI water, then

294   given a quick ~30s rinse in 1M HCl to remove surface contamination before being dried at 50°C

295   in a vacuum oven for 30 minutes. The sample surface was coated with ~10-20 nm of gold for

296   conductivity before being loaded in the instrument sample lock chamber.

297   Zircon U-Th analyses were conducted on the SHRIMP-RG (reverse geometry) ion

298 microprobe in the co-operated Stanford and U. S. Geological Survey SUMAC facility at Stanford

299 University. Analytical procedure and data reduction follows methods developed by Williams

300 (1997) and Ireland and Williams (2003). An O_2^- primary beam with accelerating voltage of 10 kV

301 was used to sputter secondary ions from the sample surface with a ~19 nA primary beam current

302 focused to ~42 μm. Prior to analysis, spots were presputtered for 60 seconds remove gold coating

303 and surface contamination from the analysis area, and the primary and secondary beams were

304 auto-tuned to maximize transmission. Seven masses were measured, including $^{90}Zr_2^{16}O$, $^{238}U^+$,

305 $^{232}Th^{12}C^+$, $^{230}Th^{16}O^+$, background measured 0.050 AMU above the $^{230}Th^{16}O^+$ peak, $^{232}Th^{16}O^+$, and

306 $^{238}U^{16}O^+$. An energy slit set to 1 mm width was employed to reduce interferences. Data were

307 collected over 8 scans per spot, for a total run time of 33 minutes, collected by magnet peak-

308 jumping on an EPT discrete-dynode electron multiplier. Mass resolution (M/ΔM) was set to

309 ~8000 for all masses, sufficient to resolve any interfering molecular species.

310   Zircon U concentration data were standardized against the well-characterized MAD-559

311 (3940 ppm U; Coble et al. 2018) and MAD-1 zircon standards (Barth and Wooden 2010) measured

312 from a separate mount that was co-loaded in the analysis chamber. $(^{238}U)/(^{232}Th)$ and

313 $(^{230}Th)/(^{232}Th)$ ratios were calculated using λ_{238} = 1.55125x10^{-7} ka^{-1} (Jaffey et al. 1971), λ_{232} =

314 4.9475x10^{-8} ka^{-1} (Steiger and Jäger 1977), λ_{230} = 0.0091705 ka^{-1} (Cheng et al. 2013). The

315 $(^{238}U)/(^{232}Th)$ was also corrected for instrument mass fractionation using early-erupted Bishop

316 Tuff (767.1±0.9 ka, Crowley et al. 2007), which is relatively high-U (1000-4000 ppm) and old

317 enough that the U-Th is in secular equilibrium. For analyses measured in this session $(^{230}Th)/(^{238}U)$

318 = 0.8461±0.0069 (1σ, n = 9, MSWD = 2.2), which is the RSF that was applied to the unknowns.

319 Data was reduced using the Microsoft Excel add-in programs Squid2.51 and Isoplot3.764 of Ken

320 Ludwig (Ludwig 2001; 2003).

321

322   4. Results

323   4.1 ^{230}Th-^{238}U ages of the LdM zircons

324   We determined the ^{230}Th-^{238}U ages of 11 rdm zircons, ranging from 18.7 ka to secular

325 equilibrium (>350 ka) (Fig. 3). Out of the 11 rdm zircon grains that were dated, four of them

326   (hereafter referred to as younger rdm zircons) have non-secular equilibrium ages that range from

327   18.7 to 47.0 ka, falling within the ^{230}Th-^{238}U ages (18.1 to 78.8 ka) previously determined for the

328   zircons from the same unit (Andersen et al. 2019). The youngest zircon age is $18.7^{+5.0}_{-4.7}$ (1SD) ka,

329   which agrees well with the eruption age of the rdm unit (19-23 ka based on field relationships).

330   The remaining seven rdm zircon grains are in secular equilibrium indicating unresolvable ages

331   that are >350 ka (hereafter older rdm zircons). The six rdm zircon grains that could not be dated

332   (hereafter no age (NA) rdm zircons) either due to the size or SHRIMP beam overlapping epoxy

333   are not included in further discussion given the difficulty in putting them in context of other data

334   without their ^{230}Th-^{238}U ages. For the rle zircons, the previously determined ^{230}Th-^{238}U ages range

335   from 14.9 to 80.8 ka, and those with MIZs found in this study are 19.7 to 48.3 ka (Andersen et al.

336   2019). No MIZ was found in the rle zircon that is in secular equilibrium.

337

338   **4.2 Major elements**

339   The major element composition of the younger rdm MIZs are all rhyolitic (75.1 to 76.6

340   wt.%) and relatively homogeneous (Fig. 4). Their composition agrees well with the tight array

341   defined by the whole rock data of the post-glacial silicic units (Hildreth et al. 2010; Andersen et

342   al. 2017). Their composition is less evolved compared to the rdm whole rock data (Hildreth et al.

343   2010; Andersen et al. 2017) and the rdm matrix glasses (Contreras et al. 2022) (Fig. S4). The

344   younger rdm MIZs agree well with the most evolved side of the compositional range defined by

345   the rdm plagioclase melt inclusions, which show significant range in SiO_2 (71 to 76 wt.%).

346   However, the younger rdm MIZs are less evolved compared to the rdm quartz melt inclusions

347   (Klug et al. 2020).

348   In contrast to the younger rdm MIZs, the major element composition of older rdm MIZs

349   are rhyodacitic to rhyolitic, significantly more heterogeneous, and for the most part do not agree

350   well with those of the rdm whole rock/melt inclusions nor with those of the post-glacial silicic

351   units (Andersen et al. 2017) (Fig. 4). The post-glacial whole rock data form a tight array of

352   chemical data, while the whole rock composition of older units (> 25 ka) is more scattered (Fig.

353   S5). Some of the older rdm MIZs agree with the composition of these older units (Hildreth et al.

354   2010). However, many of the older rdm MIZs are anomalous (e.g., those with high K_2O of > 6

13

355   wt.%) even compared to the whole rock composition of the older eruption units. While there

356   may be a tendency for CL pattern of zircons surrounding older rdm MIZs to have more complex

357   patterns (Fig. S1), clear correlation between MIZ composition and surrounding zircon CL pattern

358   were not observed.

359   Similar to the younger rdm MIZs, the major element composition of the rle MIZs agree

360   well with the trend defined by the whole rock data of the post-glacial silicic units (Andersen et al.

361   2017) (Fig. 4). The three less evolved rle MIZs are compositionally similar to the rle whole rock

362   data (Hildreth et al. 2010; Andersen et al. 2017) and rle matrix glasses (Contreras et al. 2022),

363   while the other 3 rle MIZs are more evolved (SiO_2 = 77 to 78 wt.%) (Fig. S6). The more evolved rle

364   MIZs are compositionally similar to the rle plagioclase melt inclusions, most of which are similarly

365   evolved (SiO_2 = 76 to 78 wt.% for 11 out of 12 plagioclase melt inclusions) (Klug et al. 2020).

366

367   **4.3 H_2O contents**

368   The H_2O contents of the younger rdm MIZs span 4.1 to 5.7 wt.%, and they agree well with

369   those of the rdm plagioclase melt inclusions (Klug et al. 2020) (Fig. 5). In contrast, the H_2O

370   contents of older rdm MIZs are significantly scattered (2.1 to 6.6 wt.%) compared to the range

371   observed in the rdm plagioclase melt inclusions, reaching similarly low H_2O contents as some

372   quartz melt inclusions (Klug et al. 2020) (Fig. 5). A measurement of the matrix glass adhered onto

373   an NA rdm zircon (zircon f4) yielded a distinctly lower H_2O content of 0.05 wt.% in comparison to

374   MIZs. The H_2O contents of the rle MIZs (4.3 to 6.2 wt.%) are comparable to the younger rdm MIZs,

375   although extending to slightly higher H_2O contents. These H_2O contents are comparable with

376   those in the rle plagioclase melt inclusions (5.4 to 5.8 wt.%) (Klug et al. 2020).

377

378   **4.4 Oxygen isotopic ratios**

379   Oxygen isotope ratios of the rdm zircons are homogeneous regardless of age (i.e.,

380   younger or older rdm) ($\delta^{18}O$ = 5.76 ± 0.32 ‰, 2SD) (Fig. 6a). The $\delta^{18}O$ values of younger rdm MIZs

381   are also homogeneous ($\delta^{18}O$ = 8.22 ± 0.80 ‰, 2SD), while that of older rdm MIZs is highly variable

382   ($\delta^{18}O$ = 4.1 to 8.9 ‰) (Fig. 6a). The oxygen isotopic fractionation between the glass in younger

383   rdm MIZ and host-zircon is relatively constant ($\Delta^{18}O_{MIZ-Zrn}$ = 2.59 ± 1.01 ‰, 2SD) (Fig. 6b), and

384   within uncertainty with the equilibrium zircon-melt oxygen isotopic fractionation factor (Lackey

385   et al. 2008). The equilibrium fractionation between zircon and melt is nearly constant at

386   magmatic temperatures (Lackey et al. 2008; Grimes et al. 2011; Bucholz et al. 2017). In contrast,

387   oxygen isotopic fractionation between the older rdm MIZ and host-zircon is highly variable

388   ($\Delta^{18}O_{MIZ-Zrn}$ = -1.52 to 3.22 ‰) (Fig. 6b), and some do not preserve equilibrated values from

389   magmatic conditions. The oxygen isotopic composition of the rle MIZs/zircons were not

390   determined, due to the lack of suitable oxygen isotope standard grain in the indium mount.

391

392   **4.5 Ti-in-zircon thermometry and RhyoliteMELTS**

393   Ti-in-zircon temperatures were calculated using the calibration of Ferry and Watson

394   (2007), which requires the TiO_2 activity (a_{TiO2}), SiO_2 activity (a_{SiO2}) and pressure. Following the

395   previous study on LdM zircons of Andersen et al. (2019), we first used the a_{TiO2} of 0.72 obtained

396   based on magnetite-ilmenite equilibrium (Ghiorso and Evans 2008) and an a_{SiO2} of 1 based on the

397   presence of quartz in the LdM rhyolites (Andersen et al. 2017). The effect of pressure was not

398   taken into account, but such effect is relatively small (~50ºC/10 kbar). Ti-in-zircon temperatures

399   calculated based on these a_{TiO2} and a_{SiO2} values along with the measured Ti content in zircons

400   span 708 to 839ºC (younger rdm = 708 to 792ºC, older rdm = 722 to 839ºC, rle = 724 to 796ºC).

401   These are comparable to the Ti-in-zircon temperatures previously determined for LdM zircons

402   (Andersen et al. 2019) as well as the temperature range of LdM rhyolites estimated based on the

403   Fe-Ti oxide thermometer (Andersen et al. 2017).

404

405   **4.6 Zircon trace elements**

406   The trace element composition (e.g., U, Hf, Ti, REE contents) of the younger rdm zircons

407   agree well with those that were previously observed for rdm zircons (Andersen et al. 2019) (Fig.

408   7). While it is somewhat unexpected given the anomalous major element composition of older

409   rdm MIZs (Fig. 4), the trace element composition of older rdm zircons compares well with other

410   rdm zircons (Fig. 7a). The Ti content of younger rdm zircons range from 5 to 12 ppm, and

411   correlates negatively with their Hf content that ranges from 8,500–10,700 ppm (Fig. S7). The U

412   content of the younger rdm zircons range from 353 to 1,688 ppm, which tends to correlate with

413 the bright and dark CL regions, respectively. The trace element composition of the rle zircons

414 with MIZs (U_{Zrn} = 266–557 ppm, Ti_{Zrn} = 6–12 ppm, Hf_{Zrn} = 8,100–10,700 ppm) are representative

415 of those of the larger rle zircon data set, except for the most U-rich and -depleted zircons

416 (Andersen et al. 2019). The melt in equilibrium with the zircons calculated using the zircon-melt

417 REE partition coefficients (Sano et al. 2002) are consistent with the whole rock data for the LdM

418 post-glacial units (Andersen et al. 2017) (Fig. S8).

419

5. Discussion

5.1 Post-entrapment modification of MIZs

422 Subsequent to entrapment in the host crystal, melt inclusions can be modified by

423 processes such as devitrification, crystallization of new zircon, cracking of host zircon and

424 diffusive exchange with the surrounding melt (e.g., Danyushevsky et al. 2002). However, multiple

425 lines of evidence suggests that post-emplacement processes have had minimal effects on many

426 of the MIZs from rdm and rle units, and that many of the MIZs retain major element, oxygen

427 isotopic composition, and water contents of the entrapped magmas. Post-entrapment

428 crystallization (PEC) (e.g., Kress and Ghiorso 2004) of zircon during cooling is minimal for MIZs

429 given the small concentration of Zr in the melt. For example, LdM whole rocks have a maximum

430 Zr content of 265 ppm (Hildreth et al. 2010), which limits the maximum amount of PEC of zircon

431 to < 0.05 wt.% in a MIZ, assuming Zr content of 500,000 ppm in zircon and that all Zr in the melt

432 is converted to zircon. The effect of PEC of other minerals on the composition of the MIZs in this

433 study is difficult to constrain as we did not conduct heating experiments. However, the younger

434 rdm as well as the rle MIZs in this study have minimal to no textural evidence by SEM of PEC

435 phases given their homogeneous nature (Figs. 2 and S1). Further, the agreement between the

436 major element composition of younger rdm and rle MIZs (^{230}Th-^{238}U age of host zircon < 60 ka)

437 to those of whole rock data of the post-glacial silicic units (Andersen et al. 2017), as well as those

438 of plagioclase and quartz melt inclusions from the same unit (Klug et al. 2020), suggests that PEC

439 did not have a substantial effect on the younger rdm and rle MIZ compositions (Fig. 4). In contrast,

440 the major element composition of most older rdm MIZs (^{230}Th-^{238}U age of host zircon in secular

441 equilibrium) significantly deviate from those of whole rock, and plagioclase and quartz melt

442   inclusions, which could be due to the effect of PEC. Nevertheless, the most notable difference in

443   major element composition between younger rdm and older rdm MIZs would require a

444   substantial amount of PEC (e.g., K_2O of 4.4 wt.% in younger rdm MIZ vs. 6.5 wt.% in some older

445   rdm MIZs require ~33 wt.% crystallization of quartz) if the original melts were of the same

446   composition. The lack of substantial PEC minerals in SEM images of the older rdm MIZs does not

447   support such large amount of PEC (Figs. 2 and S1). Together with the old age (>350 ka) of the

448   older rdm MIZs, a more likely explanation is that they formed from a parental melt that formed

449   under magmatic conditions unrelated to those that produced the younger rdm and rle MIZs and

450   other LdM units.

451   Melt inclusions can record the pre-eruptive volatile contents of magmas. However, after

452   entrapment, volatiles can sometimes diffuse into or out of melt inclusions through the host

453   mineral (e.g., Qin et al. 1992). There are so far no experimental measurements of H diffusion

454   coefficient in zircon under conditions relevant to the LdM zircons (e.g., fO_2 conditions). In the

455   LdM MIZs, we observe a negative correlation between the degree of differentiation (SiO_2) and

456   H_2O contents of MIZs (Fig. 5) that is consistent with those observed in plagioclase and quartz melt

457   inclusions. This negative correlation has been interpreted to suggest decompression-driven

458   fractional crystallization and H_2O degassing as the rdm magma ascended from deeper to

459   shallower portion of the LdM reservoir (Klug et al. 2020). The preservation of such negative

460   correlation in the rdm MIZs strongly suggests the retention of MIZ H_2O contents since the time

461   of entrapment, as diffusive exchange would decouple H_2O from SiO_2 in the MIZs. Some older rdm

462   MIZs (>350 ka) are characterized by low H_2O contents for a given SiO_2 (Fig. 5), and may indicate

463   instances of H_2O leakage from these MIZs. With these exceptions aside, we infer that the negative

464   correlation between SiO_2 and H_2O contents to indicate that the MIZs in this study were not

465   significantly impacted from diffusive equilibration of H through the host zircon since the time of

466   entrapment.

467

468   **5.2 Identification of xenocrystic rdm zircons/MIZs (older rdm)**

469   The older rdm zircons that are in secular equilibrium (>350 ka) host MIZs that are

470   anomalous in composition (Fig. 4). Their compositions do not agree with those of the rdm unit

17

471   nor other whole rock data of the post-glacial silicic units and older units (Hildreth et al. 2010;

472   Andersen et al. 2017). The older rdm MIZs are generally low in FeO and MgO and also show

473   significantly more variable CaO, TiO_2, as well as H_2O contents for a given SiO_2 content compared

474   to the younger rdm and rle MIZs and LdM whole rock data (Figs. 4 and 5). Three older rdm MIZs

475   have significantly higher K_2O content than younger rdm and rle MIZs as well as LdM whole rock

476   (Fig. 4). These high K_2O older rdm MIZs have anomalously low $\delta^{18}O$ values that are not in isotopic

477   equilibrium with the host zircon (Fig. 6b). While the distinct major element composition could in

478   part be due to post-entrapment crystallization of certain phases, high K_2O contents and

479   anomalously low $\delta^{18}O$ observed in some MIZs are difficult to explain by such process. Taken

480   together with their secular equilibrium ages (>350 ka), we hypothesize that older rdm

481   zircons/MIZs are xenocrystic in origin and that the MIZs record older exotic melt compositions

482   that formed under magmatic conditions unrelated to those that produced the rdm and rle

483   eruptions. The highly variable H_2O content of older rdm MIZs also supports this hypothesis. Our

484   observation shows the importance of age dating the host zircon in order to avoid xenocrystic

485   zircons that may host MIZs with chemical composition that is irrelevant to the magmatic system

486   of interest. In terms of the origin of the older rdm zircons, they may have originated from deeper

487   granites that are represented by crustal xenoliths found in the pyroclastic flow facies of the rdm

488   unit. These are exceptionally large (up to ~1 m) crustal debris with heterogeneous lithologies that

489   could be Pliocene-Miocene plutonic rocks that housed the magmatic precursor to the more

490   recent LdM system, analogous to those observed in the Risco Bayo-Huemul plutonic complex 20

491   km west of the LdM system (Schaen et al. 2018; Schaen et al. 2021). The other post-glacial units

492   including the rle do not contain such granitoid xenoliths. The rdm unit is exceptional in this regard,

493   which explains the uniquely high abundance of secular equilibrium age zircons in the rdm units

494   compared to other units including the rle unit.

495

496   **5.3 Major element composition and H_2O contents of the younger rdm and rle MIZs:**

497   **Implications for the LdM magmatic system**

498   In contrast to the older rdm zircons and MIZs, the geochemical data of the younger rdm

499   zircons and MIZs are consistent with their formation from the active magmatic system that

500   underlies the LdM. The ^{230}Th-^{238}U ages of $18.7^{+5.0}_{-4.7}$ to $47.0^{+4.0}_{-3.9}$ (1SD) ka for the younger rdm

501   zircons agrees with the previously determined ^{230}Th-^{238}U ages (18.1 to 78.8 ka) of the rdm unit

502   zircons (Andersen et al. 2019). All younger rdm MIZs are in oxygen isotopic equilibrium with their

503   host zircon (Fig. 6b). The major element compositions of younger rdm MIZs are akin to those of

504   the whole rock data for the rdm unit as well as other post-glacial LdM units (Hildreth et al. 2010;

505   Andersen et al. 2017), matrix glasses (Contreras et al. 2022), and plagioclase/quartz melt

506   inclusions (Klug et al. 2020) (Figs. 4 and S4). The SiO$_2$ contents of these younger rdm MIZs are

507   consistent with the predicted SiO$_2$ content (>70 wt.%) above which the LdM whole rocks become

508   zircon saturated based on their Zr content and zircon saturation models of Watson and Harrison

509   (1983) and Boehnke et al. (2013) (Andersen et al. 2017). In addition, the trace element

510   concentrations (e.g., REE, U, Hf, Ti contents, Eu/Gd) of younger rdm zircons are also within those

511   that were previously observed for rdm zircons (Andersen et al. 2019) (Fig. 7). Following the same

512   reasoning, rle zircon trace element composition and ^{230}Th-^{238}U ages (Andersen et al. 2019) (Fig.

513   7) and the rle MIZ composition (Figs. 4 and S6) supports the notion of their formation from the

514   magmatic system that underlies the LdM. Hence, the younger rdm and rle zircons in this study

515   formed from melts in a growing crystal mush over a significant part of its 60 kyr history (based

516   on the oldest zircon ages of Andersen et al. (2019)), and the MIZs hosted in these zircons record

517   the compositions and storage depths of the zircon-saturated regions within the crystal mush melt

518   over time. In order to correlate the ^{238}U–^{230}Th age from the host zircon with the MIZ composition,

519   uncertainties associated with the placement of the age spots relative to the location of the MIZs

520   within the host zircon were considered. We used the CL images of the host zircon (Fig. S1-1) to

521   determine if an age spot can be considered to date the (1) age of the MIZ entrapment (when the

522   age spot is directly in the same CL domain as the MIZ), or should rather be considered to date

523   the (2) minimum or (3) maximum age of the MIZ entrapment (depending on whether the age

524   spot is in a CL domain that is further away from (i.e., min. age) or closer to (i.e., max. age) the

525   zircon core than the MIZ (refer to the caption of Fig. 8 for details)).

526   The younger rdm and rle MIZ compositions record relatively homogeneous crystal mush

527   melt composition during its buildup (Fig. 8) that is consistent with the post-glacial silicic whole

528   rock data (Fig. 4). However, there are compositional differences between the younger rdm and

529   rle MIZs. The younger rdm MIZs are on average less differentiated (e.g., lower SiO_2, higher Al_2O_3

530   and MgO) than the rle MIZs (Fig. 8), and this difference is observed from at least ~30 kyr before

531   eruption until close to the eruption ages of both units (19 to 23 ka) (Fig. 8). Less evolved rdm MIZ

532   compared to rle MIZ is consistent with the hypothesis that the rdm crystal mush was better

533   connected to the deeper mid-crustal plumbing system than the rle crystal mush, as proposed by

534   Klug et al. (2020) based on the less evolved rdm plagioclase melt inclusion with deeper

535   entrapment depths as compared to those of rle. While the plagioclase melt inclusions were

536   entrapped only decades to centuries before eruption (Andersen et al. 2018), MIZs record a

537   persistent difference between rdm and rle going back to ~30 kyr before eruption, suggesting the

538   long-term connection of the rdm crystal mush to deeper depths (higher T and lesser degree of

539   plagioclase/zircon fractionation) than that of the rle.

540   The storage depths of younger rdm MIZs are 1.1 to 2.8 kbars or 4.0 to 10.5 km (Fig. 9),

541   based on their H_2O contents, assumed range of CO_2 content of 0 to 570 ppm (based on the

542   plagioclase-hosted melt inclusions from the rdm unit), and the MagmaSat model of Ghiorso and

543   Gualda (2015) implemented in the VesiCal v1.01 software (Iacovino et al. 2021). There is no clear

544   correlation between the storage depth and the MIZ entrapment age (Fig. 9). The storage depth

545   is consistent with those of the silicic plagioclase-hosted melt inclusions from the rdm unit (Klug

546   et al. 2020) that formed decades to centuries before the eruption of the rdm unit based on the

547   disequilibrium trace element profiles (Andersen et al. 2018). Similar to the rdm MIZs, the rle MIZs

548   record storage depths of 1.4 to 2.8 kbars or 5.3 to 10.4 km (assuming MIZ CO_2 of 25 to 344 ppm

549   based on the plagioclase-hosted melt inclusions from the rle unit) that matches well with those

550   recorded by the rle plagioclase melt inclusions (Klug et al. 2020). The storage depth of rle MIZs

551   appears to decrease through time (Fig. 9), but the significance of this trend is unclear given the

552   small number of MIZs. The agreement between the storage depths of MIZs and those of

553   plagioclase-hosted melt inclusions suggests that the storage depths of evolved melts that are

554   zircon- (+plagioclase- ± quartz-) saturated were relatively constant from the time of MIZ

555   entrapment (younger rdm and rle zircon formation ages of 18.7 to 47.0 ka and 19.7 to 55.8 ka,

556   respectively) until the time of rdm and rle eruption (plagioclase age of decades to centuries

557   before eruption at 19 to 23 ka for rdm and 19 ± 0.4 ka for rle). The storage depth of 1.1 to 2.8

558 kbars recorded by younger rdm and rle MIZs are consistent with the optimal emplacement
559 window (2.0 ± 0.5 kbar) of silicic magma reservoir growth, storage, and eruptibility based on the
560 thermomechanical model of Huber et al. (2019).
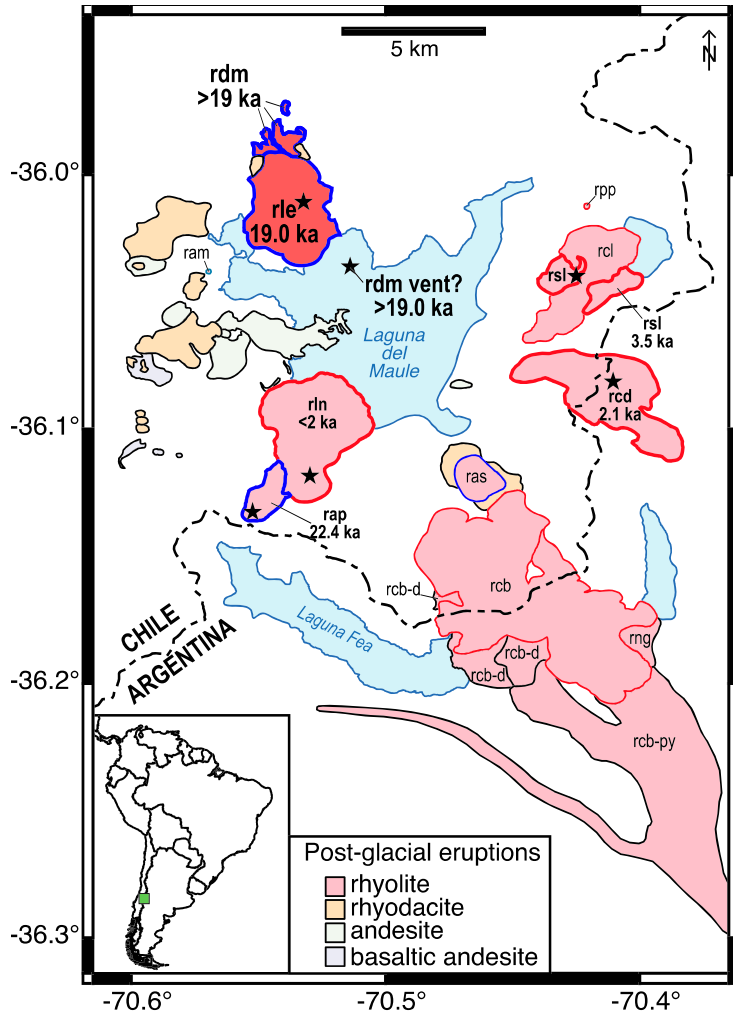
561

562 **5. Conclusion**

563   The study of MIZs from the Laguna del Maule volcanic field provides unique insights into
564 the structure and evolution of silicic magmatic systems. MIZs extends the record of magma
565 compositions back to ~30 kyr before the eruption, providing important constraints on the age,
566 storage depth, temperature, and composition of magmas. We observe a long-term difference in
567 zircon-saturated melt composition between the rdm and rle eruption units, with the rdm MIZs
568 indicating a less evolved crystal mush than that of the rle. These findings suggest the that since
569 ~30 kyr before eruption, the rdm crystal mush was better connected to a deeper and more
570 primitive magma body than the rle crystal mush. The correlation between SiO_2 and H_2O contents
571 observed in the MIZs suggests that the H_2O content of the MIZs are not significantly affected by
572 diffusion of H through the host zircon. The rdm and rle MIZs storage depths of 1.1 to 2.8 kbars
573 recorded by their H_2O contents are consistent with the optimal emplacement window (2.0 ± 0.5
574 kbar) of silicic magma reservoir growth, storage, and eruptibility based on thermomechanical
575 model of Huber et al. (2019).

6. Acknowledgements

7. Figures

Figure 1. Simplified map of the Laguna del Maule lake basin and the distribution of post-glacial eruptive units and vents (black stars). Lava flows and pyroclastic flows/falls that erupted in the early post-glacial period (22.5–19 ka) are outlined in blue, while those that erupted in the Holocene (8.0–1.8 ka) are outlined in red. Those that erupted in the interim are outlined in black. Eruptive units for which MIZ data were obtained (rdm and rle units in the northwest) are highlighted with darker red fill. Map is modified from Hildreth et al. (2010) and Andersen et al. (2019). The green square in the inset shows the location of Laguna del Maule in the southern Andes.
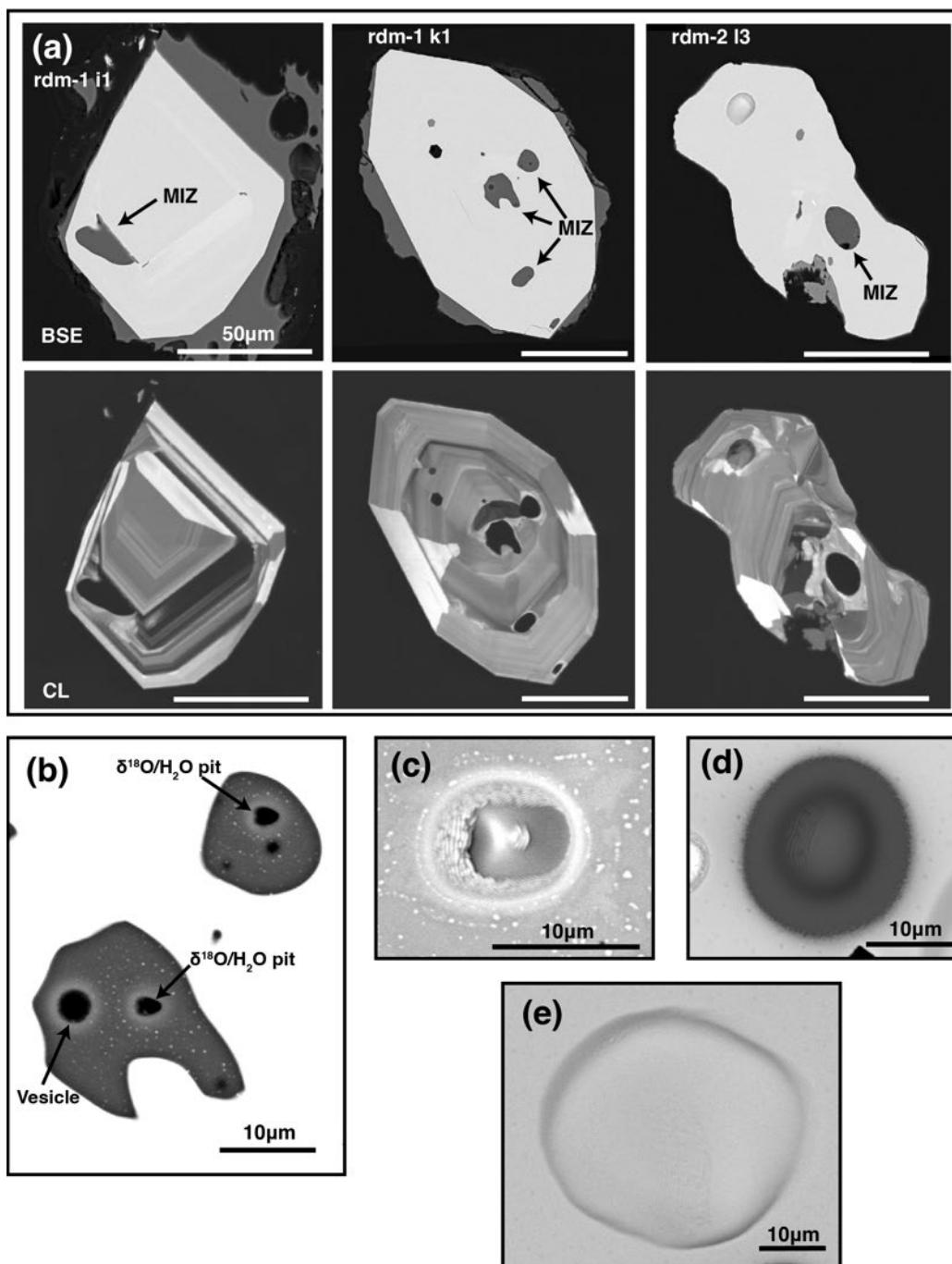
Figure 2. (a) BSE and CL images of representative MIZs/host zircons (scale bars = 50 μm). (b) BSE image of SIMS pits and Cs spatter from the analyses of $\delta^{18}O/H_2O$ of the MIZ (~3 μm diam.). (c) and (d) BSE images of SIMS pits from the analyses of $\delta^{18}O$ (~10 μm diam.) and trace element (~13 μm diam.) of the zircons, respectively. (e) BSE image of a SHRIMP pit from the $^{238}U–^{230}Th$ age dating of the zircons (~40 μm diam.).
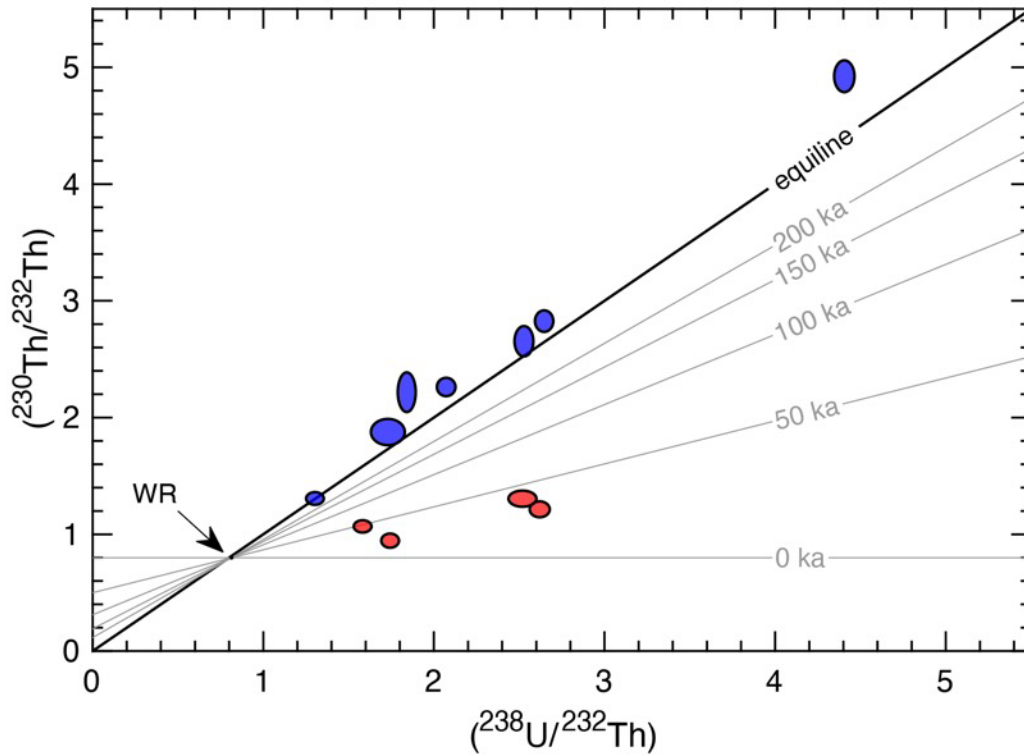
Figure 3. $^{238}U–^{230}Th$ isochron diagram for zircons from the rdm unit of the LdM. Each ellipse represents a SHRIMP-RG analysis of a spot in separate zircon grains. Error ellipses are 1SD. Red ellipses are analyses on the younger rdm zircons (non-secular equilibrium ages), while the blue ellipses are analyses of older rdm zircons (secular equilibrium ages). The small black dot represents the whole rock composition used to calculating the model ages (average of post-glacial rhyolite whole rock data from Andersen et al. (2017)). The heavy black line represents the equiline, while the gray lines represent isochrons of ages from 0 to 200 ka. Some older rdm zircons plot above the equiline, which is likely due to the primary beam overlapping with the epoxy that causes elevated $^{230}ThO^+$ background.
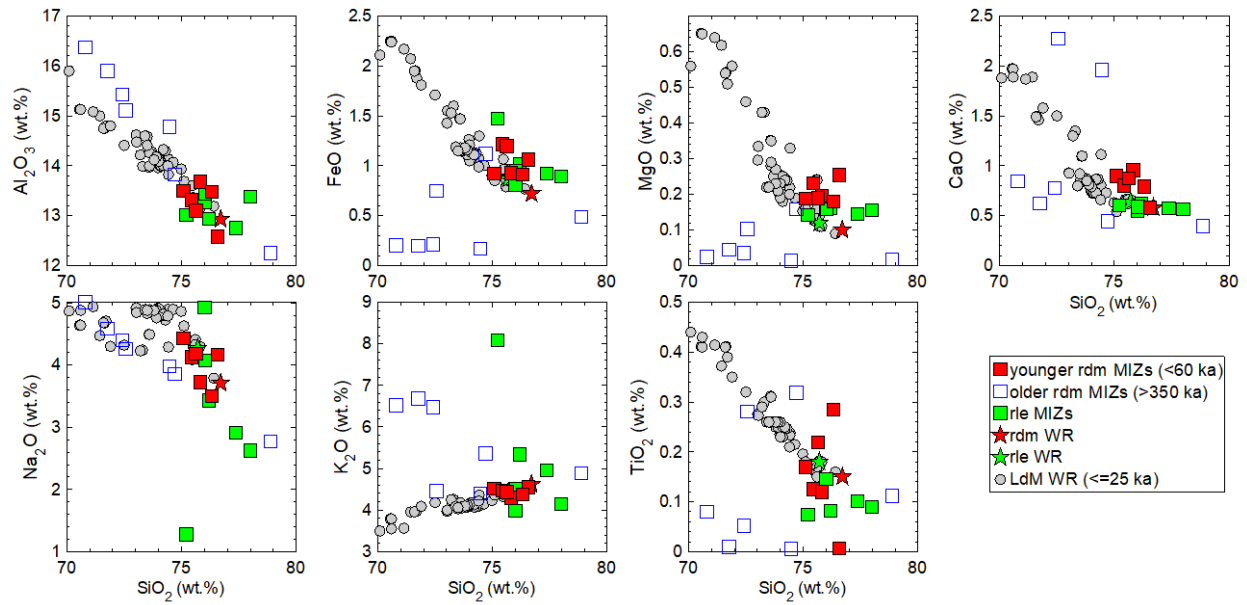
Figure 4. Harker diagrams showing the major element composition of the rdm and rle MIZs and correlated whole rock compositions. Whole rock data of younger units (<=25 ka) are from Andersen et al. (2017), Hildreth et al. (2010), and Contreras et al. (2022). MIZ compositions are normalized to 100% on anhydrous basis to allow direct comparison with the whole rock data. The matrix glass, and melt inclusions in plagioclase and quartz, and the whole rock composition of older units (> 25 ka) are not shown for clarity.

620
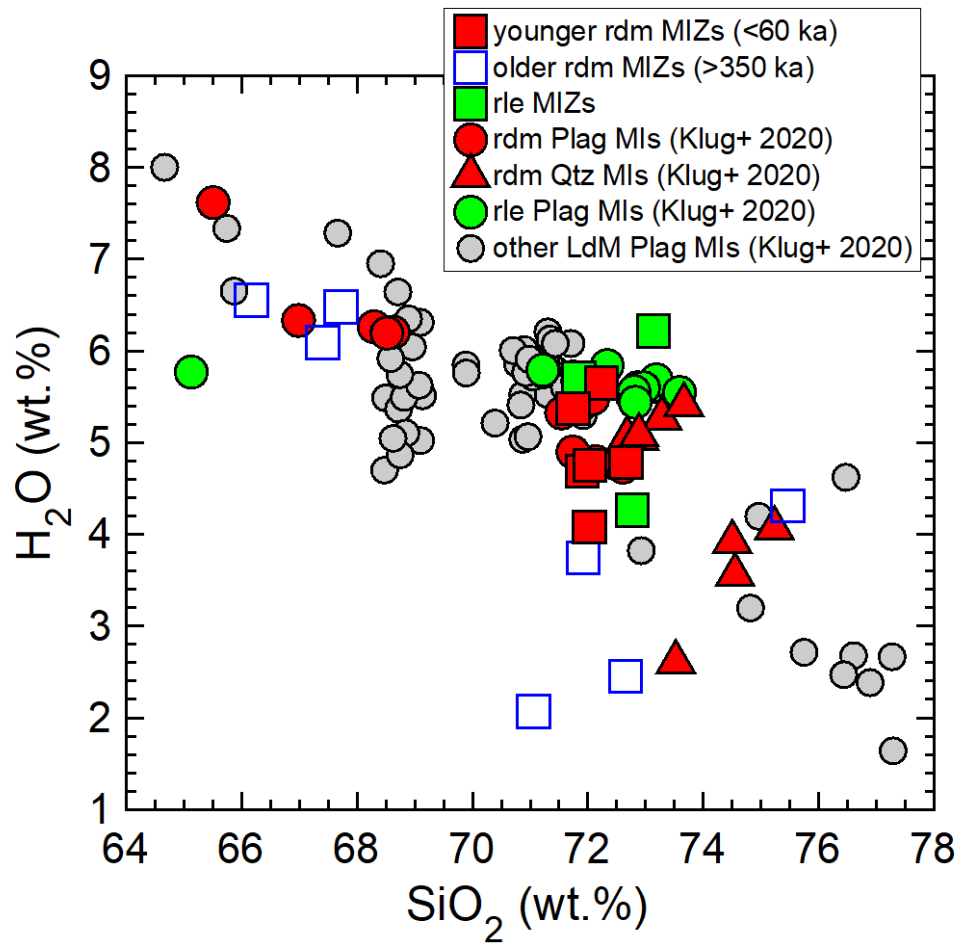
Figure 5. H_2O and SiO_2 contents of the rdm and rle MIZs along with plagioclase and quartz melt
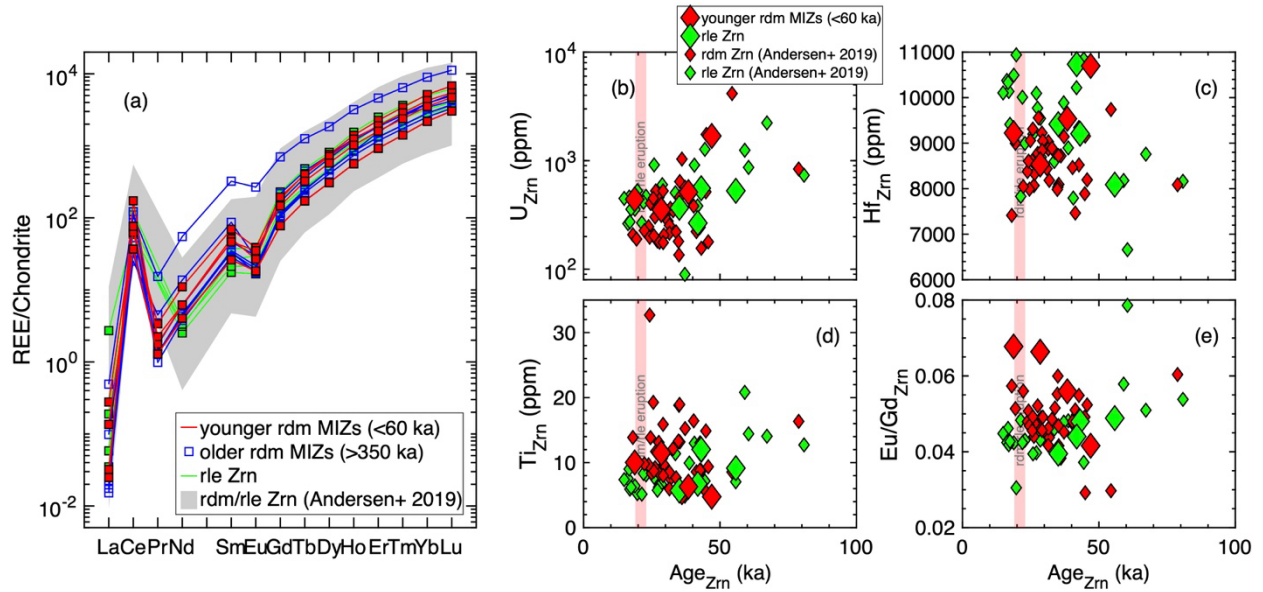inclusions (Klug et al. 2020).

623
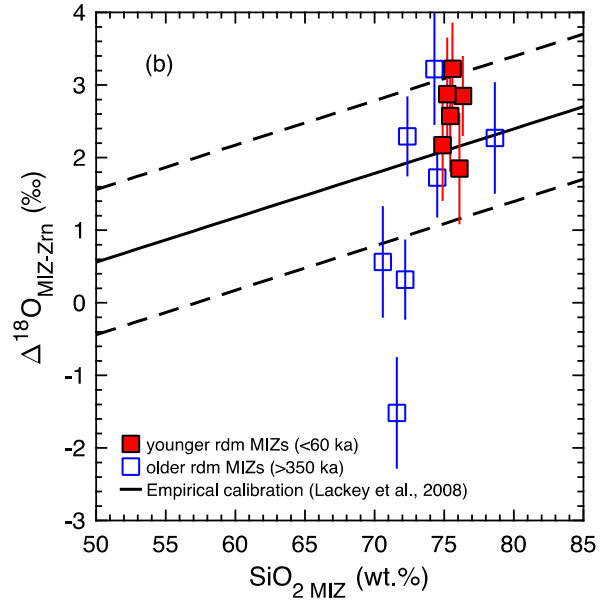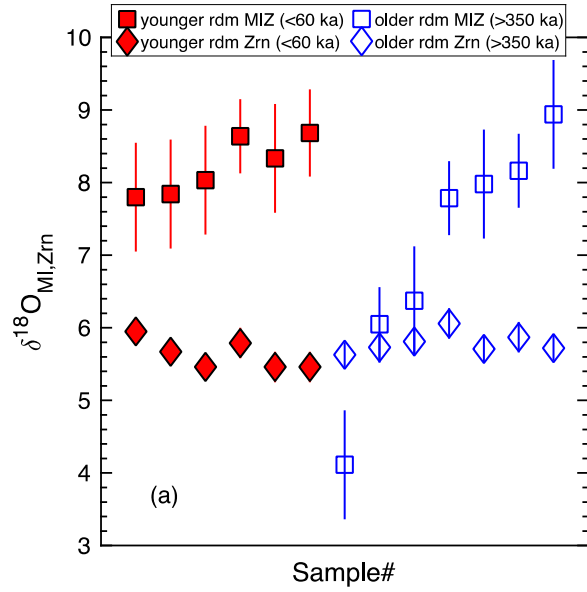
624　Figure 6. (a) $\delta^{18}O$ of the MIZ (squares) and zircon host (diamonds). (b) $\Delta^{18}O_{MIZ\text{-}Zrn}$ vs. SiO_2 content
625　of the MIZ. In (b), the dashed line shows the predicted melt-zircon equilibrium isotopic
626　fractionation (Valley et al. 2005; Lackey et al. 2008).

Figure 7. (a) Chondrite normalized REE pattern and (b) U, (c) Hf, (d) Ti, and (e) Eu/Gd vs. [238]U–[230]Th ages of the rdm and rle zircons. In (a) the gray field shows the rdm and rle zircon REE data from Andersen et al. (2019). In (b, c, d, and e), older rdm zircons are not shown given their secular equilibrium ages. The large symbols are from this study, while the small symbols are rdm and rle zircon trace element data from Andersen et al. (2019). The vertical light-red bar shows the eruption age of rdm and rle units (Andersen et al. 2017).
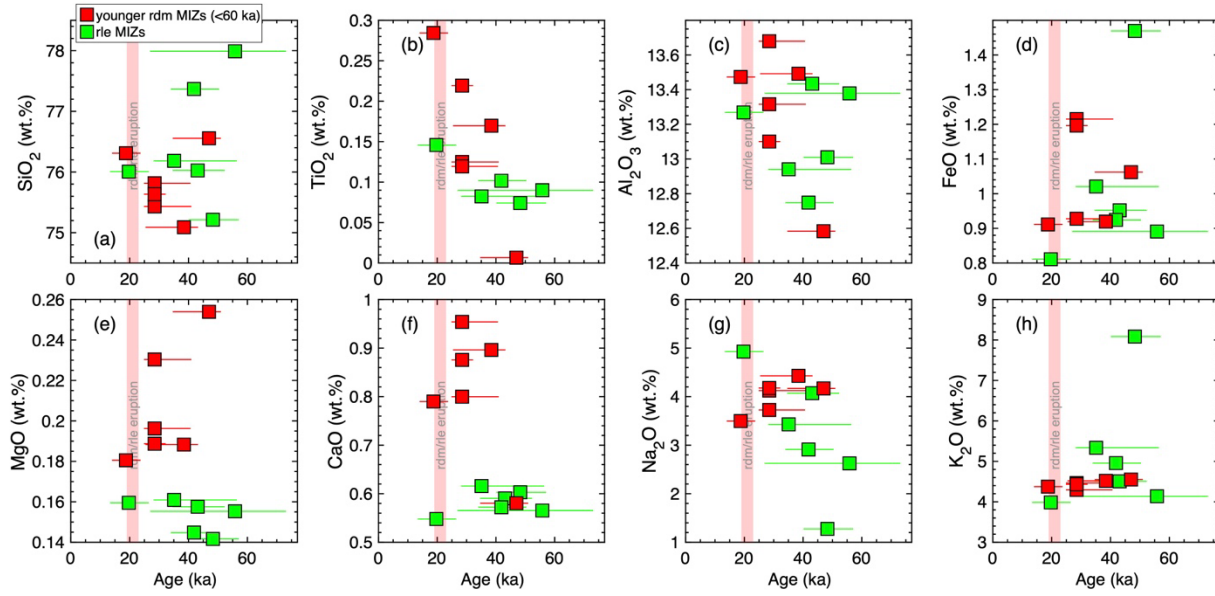
Figure 8. Major element composition of the rdm and rle MIZs vs. their entrapment ages estimated based on the ^{238}U–^{230}Th age data of the host zircons. The vertical light-red bar shows the eruption age of rdm and rle units (Andersen et al. 2017). As discussed in section 5.3, some ^{238}U–^{230}Th age spot should be considered to be the minimum (i.e., age spot in CL domain further away from zircon core than that of the MIZ) or maximum (i.e., age spot in CL domain closer to zircon core than that of the MIZ) entrapment ages of the MIZs. In such cases, we estimated the maximum or minimum MIZ entrapment ages based on the mean age difference between the zircon rim and interior ages of the rdm (8.5 kyr) and rle (13.9 kyr) zircons (Andersen et al. 2019). For example, if the age spot is in a CL domain that is closer to the zircon core than the CL domain that the MIZ is in (e.g., rdm-1 i1, Fig. S1-1), the ^{238}U–^{230}Th age $(47.0^{+4.0}_{-3.9}$ ka) was considered the maximum age of MIZ entrapment and the minimum age was estimated by subtracting the mean age difference between the zircon rim and interior ages of the rdm (8.5 kyr) zircons (Andersen et al. 2019) from the negative uncertainty of the ^{238}U–^{230}Th age (entrapment age = $47.0^{+4.0}_{-12.4}$ ka).

651
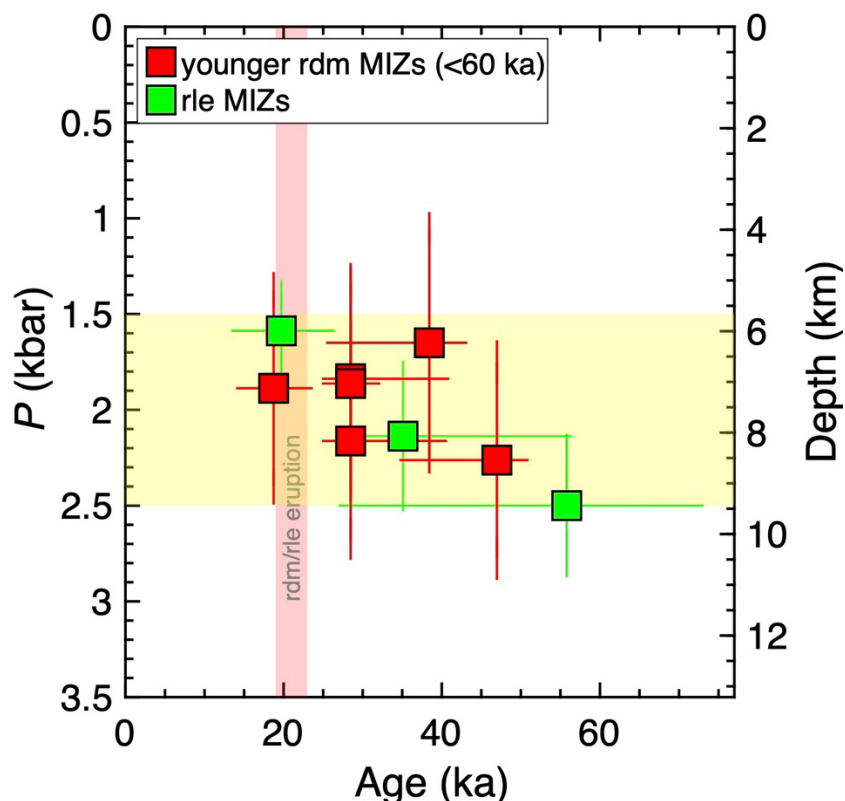
Figure 9. Storage pressures of rdm and rle MIZs vs. their entrapment ages estimated based on the ^{238}U–^{230}Th age data of the host zircons. The pressures were calculated based on the MIZ H_2O contents, ranges of MIZ CO_2 content assumed based on plagioclase-hosted melt inclusion data (Klug et al. 2020) (0 to 570 ppm and 25 to 344 ppm for rdm and rle MIZs respectively) and the MagmaSat model of Ghiorso and Gualda (2015) implemented in the VesiCal v1.01 software (Iacovino et al. 2021). The vertical light-red bar shows the eruption age of rdm and rle units (Andersen et al. 2017). The horizontal light-yellow bar indicates the optimal emplacement window (2.0 ± 0.5 kbar) of silicic magma reservoir growth, storage, and eruptibility based on thermomechanical model of Huber et al. (2019). Depth on the right axis is calculated with a crustal density of 2,700 kg/m^3. For the description of the uncertainties in the MIZ entrapment ages, refer to section 5.3 and caption of Fig. 8.
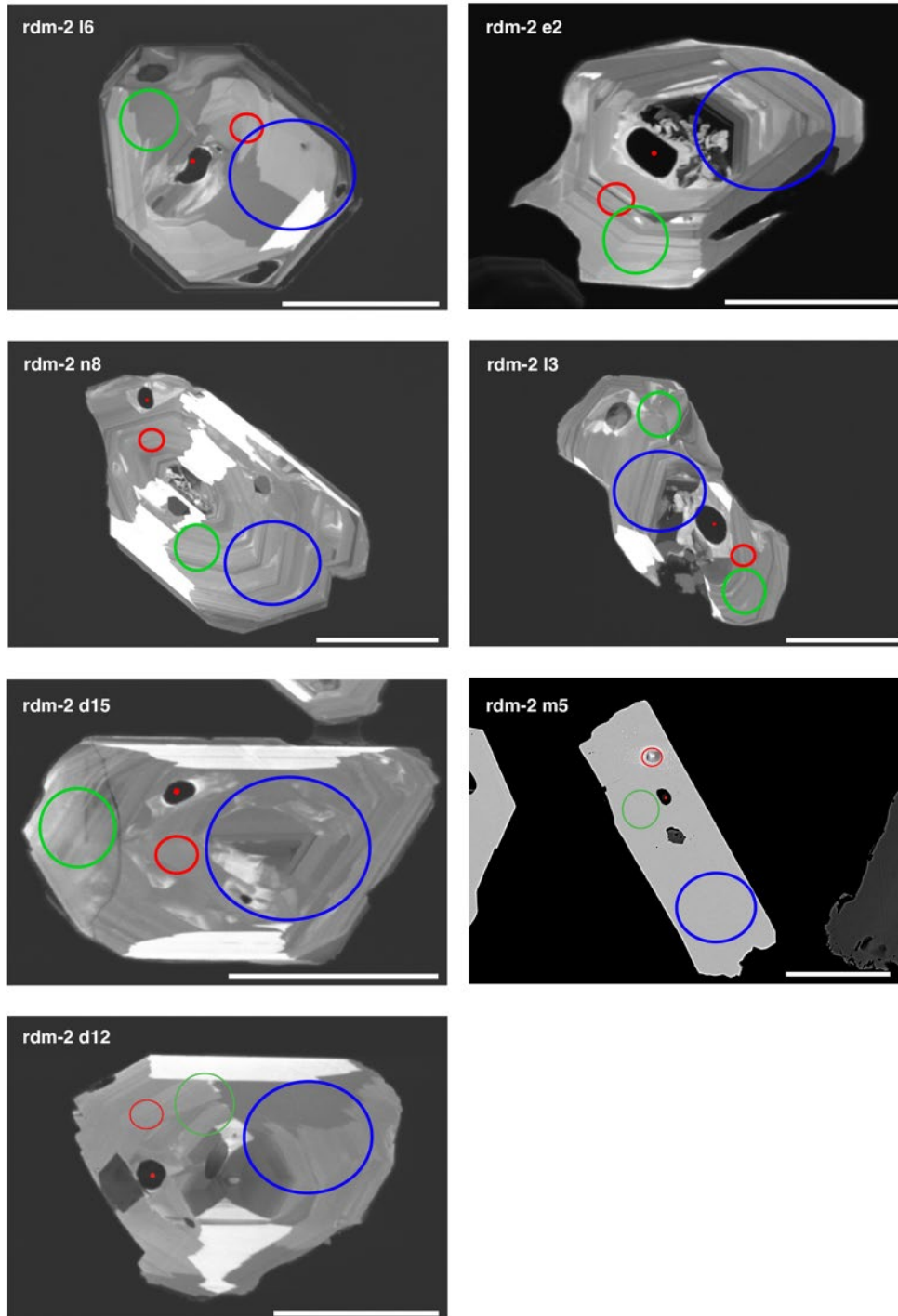
Supplementary figures

664
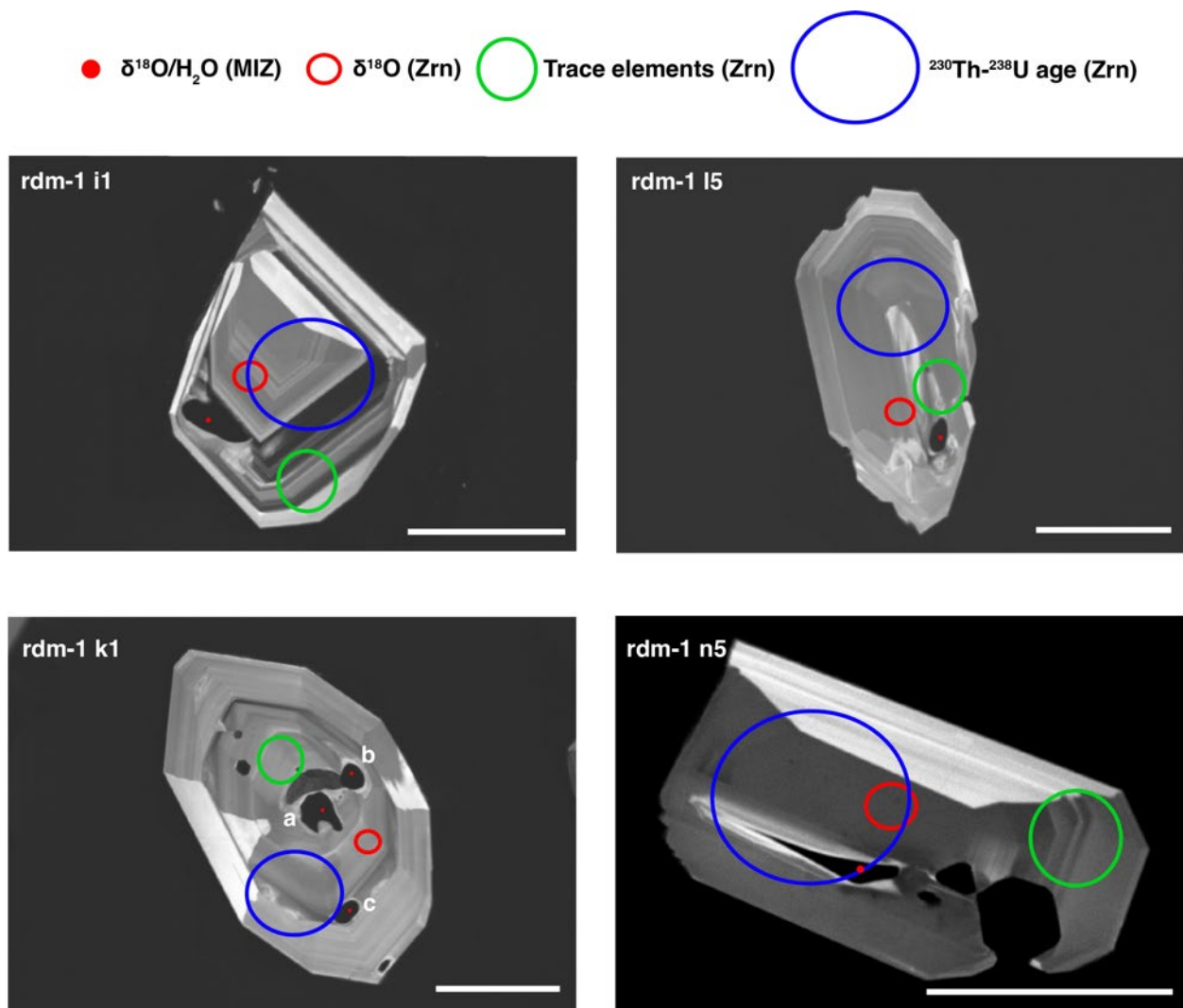
665
666 Figure S1-1. CL images of younger rdm zircons (scale bars = 50 μm). Red dots indicate locations
667 of SIMS pits from the analyses of $\delta^{18}O/H_2O$ of the MIZs, while the red and green circles indicate
668 those from the $\delta^{18}O$ and trace element analyses of the zircons, respectively. Blue circles
669 indicate locations of SHRIMP pits from the ^{230}Th-^{238}U age dating of the zircons.

Figure S1-2. CL images of older rdm zircons (scale bars = 50 μm). Red dots indicate locations of SIMS pits from the analyses of $\delta^{18}O/H_2O$ of the MIZs, while the red and green circles indicate those from the $\delta^{18}O$ and trace element analyses of the zircons, respectively. Blue circles indicate locations of SHRIMP pits from the ^{230}Th-^{238}U age dating of the zircons.

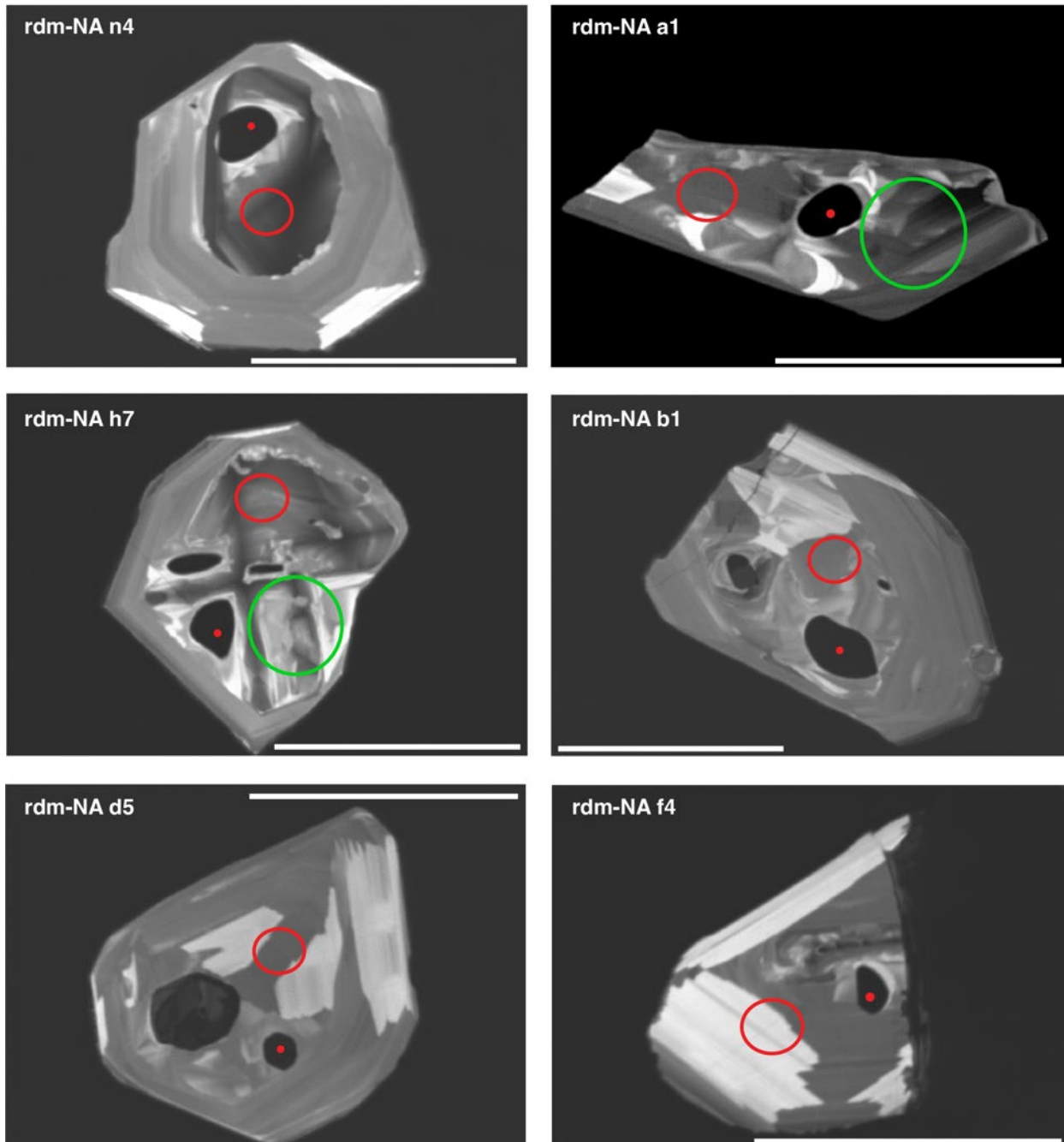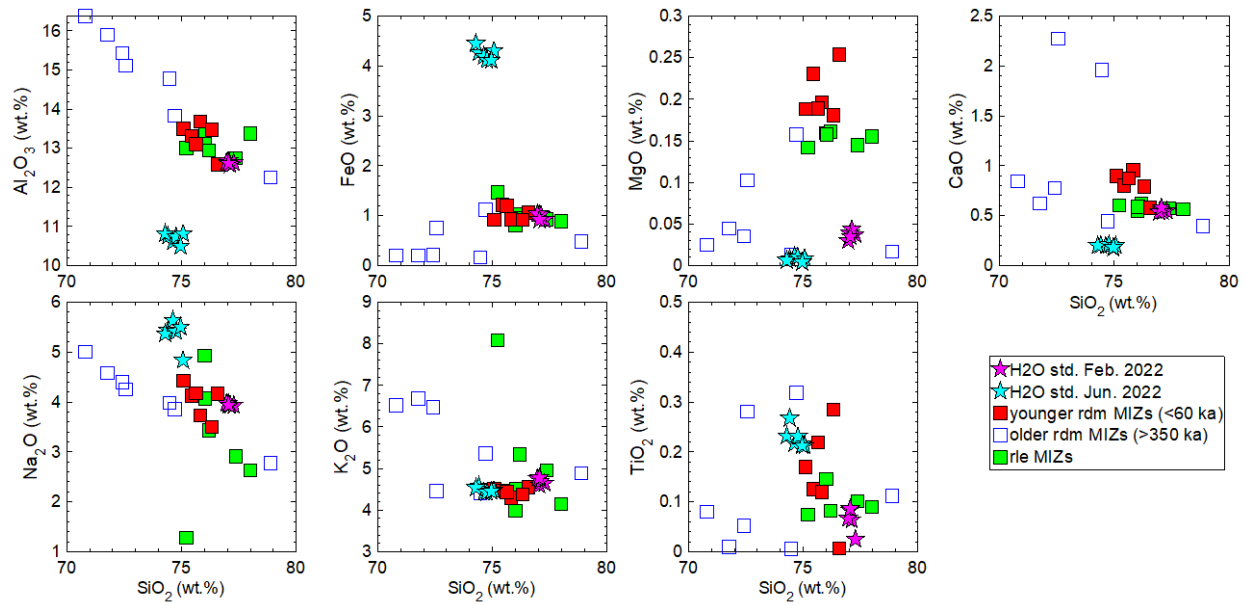Figure S1-3. CL images of rdm zircons with no ^{230}Th-^{238}U ages (no age rdm zircons) (scale bars = 50 μm). Red dots indicate locations of SIMS pits from the analyses of δ^{18}O/H_2O of the MIZ, while the red and green circles indicate those from the δ^{18}O and trace element analyses of the zircons, respectively.

680
681 Figure S2. Harker diagrams showing the major element composition of the rdm and rle MIZs
682 and the rhyolitic glasses standards with known H_2O concentrations (Newman et al. 1986; Singer
683 et al. 2014b; Klug et al. 2020) that was used for SIMS H_2O calibration.
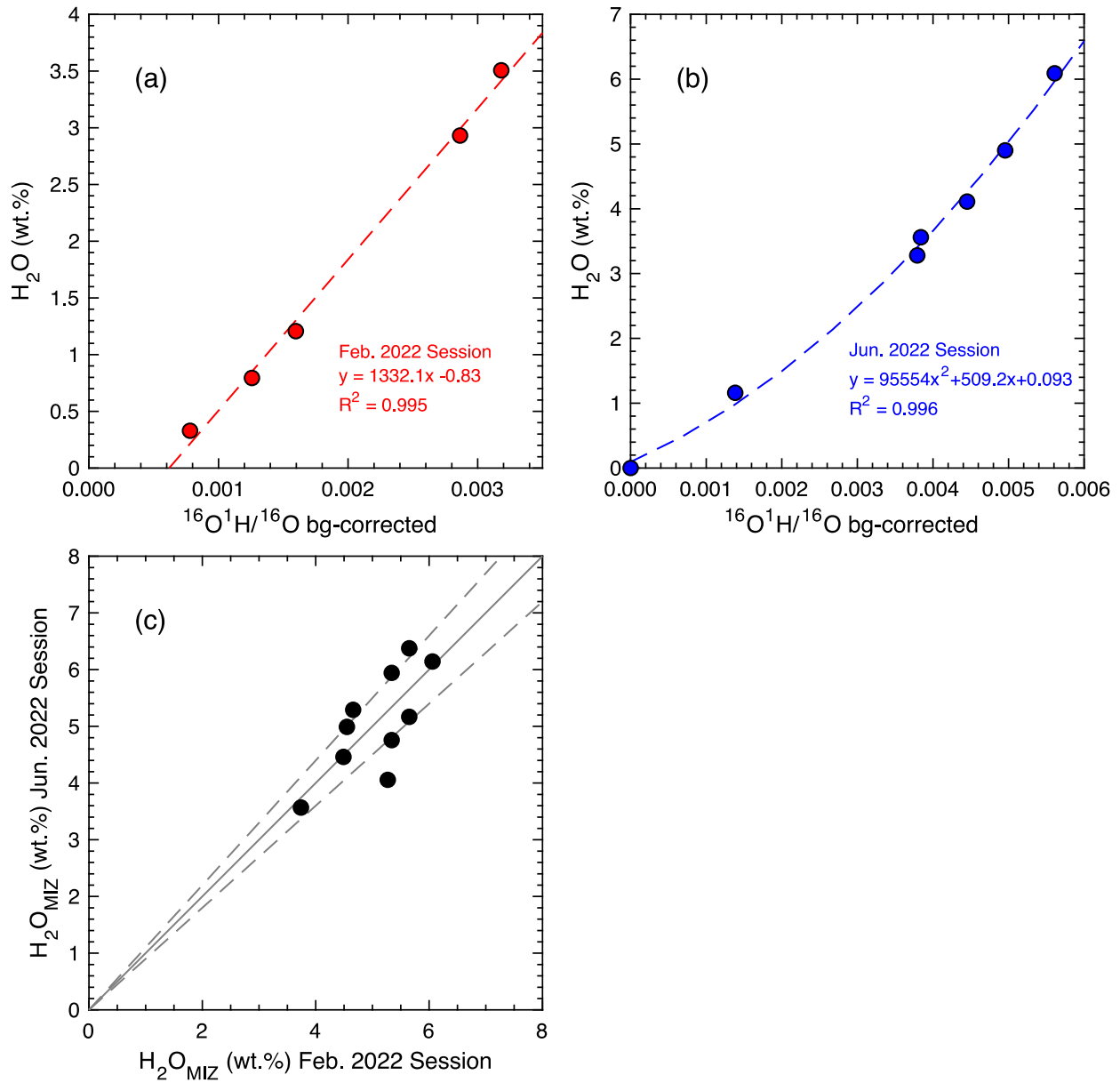
Figure S3. SIMS H_2O calibration curves from (a) February 2022 and (b) June 2022, and (c) comparison of H_2O contents measured in identical MIZs measured during the two sessions. In (c), the solid line is a 1:1 line and the dashed lines show ± 10% deviation from the 1:1 line.
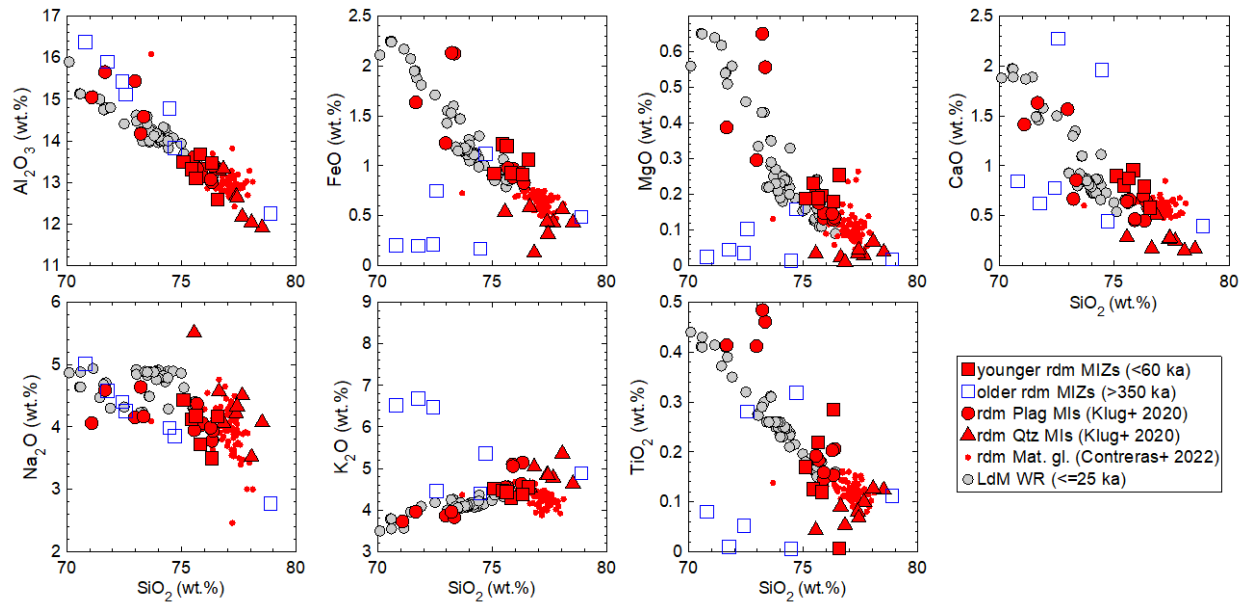
Figure S4. Harker diagrams showing the major element composition of the rdm MIZs and correlated matrix glass data (Contreras et al. 2022), and melt inclusions in plagioclase and quartz data (Klug et al. 2020). Whole rock data of younger units (<=25 ka) from Andersen et al. (2017) and Hildreth et al. (2010) are also shown. MIZ and melt inclusions in plagioclase and quartz compositions are normalized to 100% on anhydrous basis to allow direct comparison with the whole rock data (and matrix glass that is dehydrated through the eruption process).
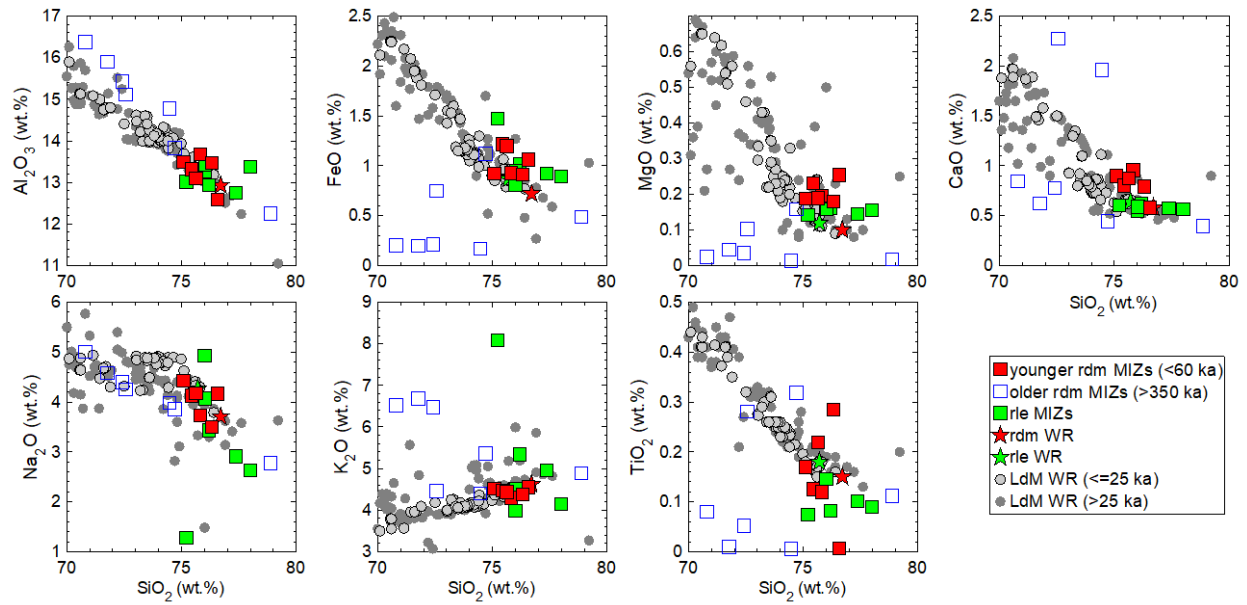
696
697 Figure S5. Harker diagrams showing the major element composition of the rdm and rle MIZs
698 and correlated whole rock compositions. Whole rock data of younger units (<=25 ka) are from
699 Andersen et al. (2017), Hildreth et al. (2010), and Contreras et al. (2022) and those of older
700 units (>25 ka) are from Hildreth et al. (2010). MIZ compositions are normalized to 100% on
701 anhydrous basis to allow direct comparison with the whole rock data.

38
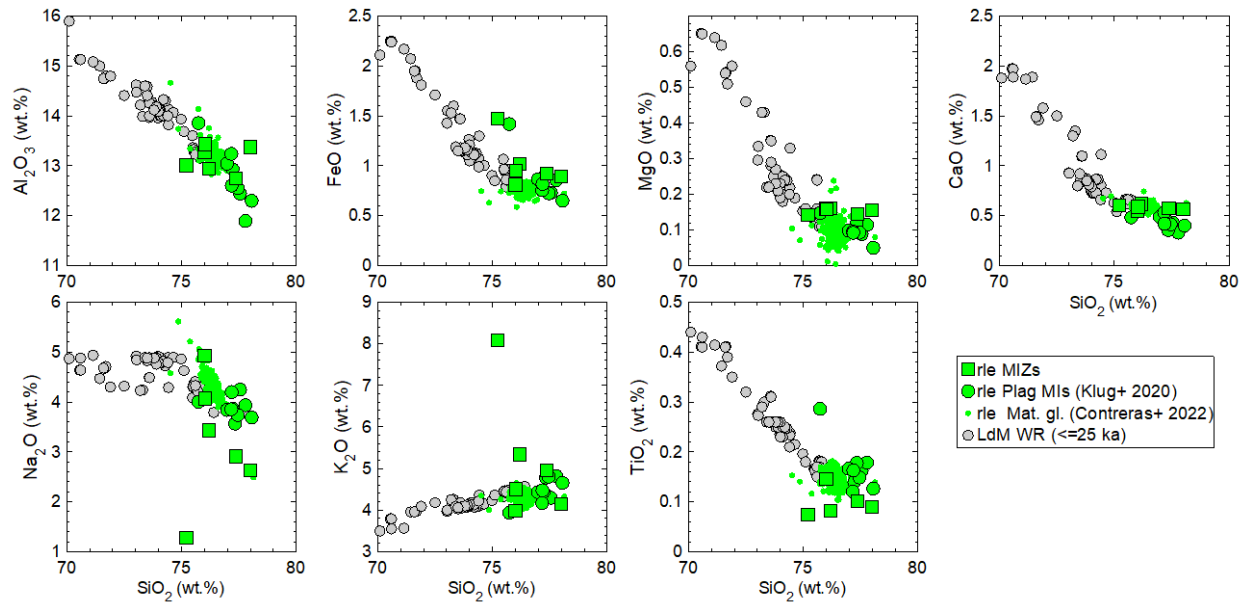
702
703 Figure S6. Harker diagrams showing the major element composition of the rle MIZs and
704 correlated matrix glass data (Contreras et al. 2022), and melt inclusions in plagioclase data (Klug
705 et al. 2020). Whole rock data of younger units (<=25 ka) from Andersen et al. (2017) and
706 Hildreth et al. (2010) are also shown. MIZ and melt inclusions in plagioclase compositions are
707 normalized to 100% on anhydrous basis to allow direct comparison with the whole rock data
708 (and matrix glass that is dehydrated through the eruption process).

709
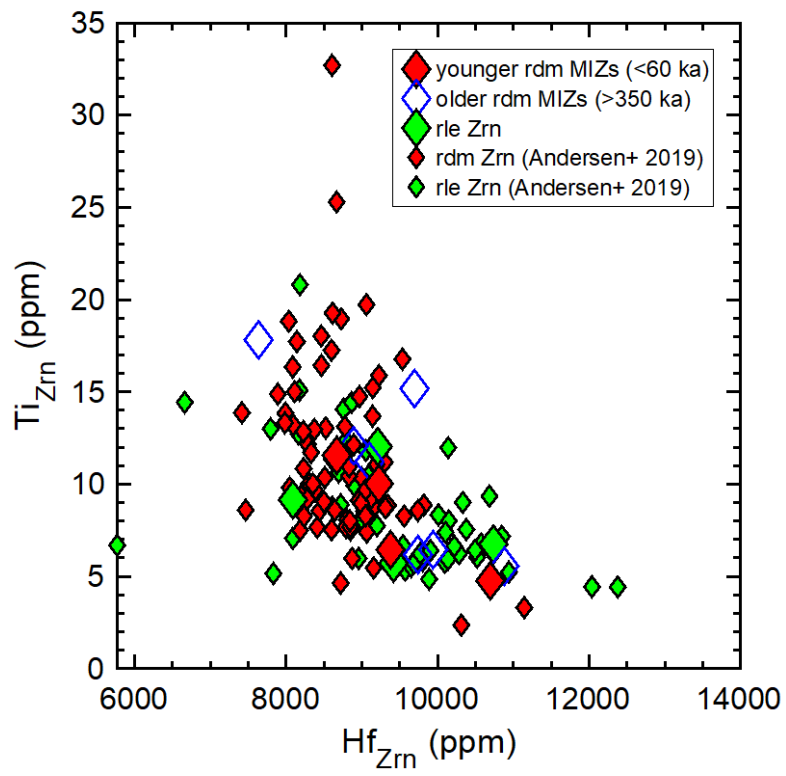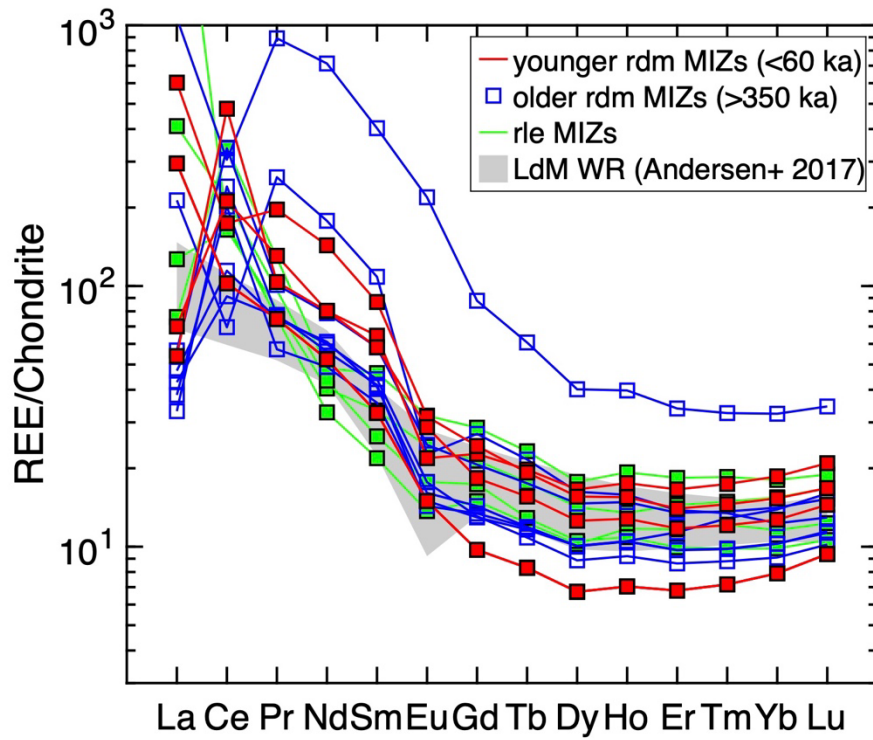710   Figure S7. Ti vs. Hf of the rdm and rle zircons.

711

712 Figure S8. Chondrite normalized REE pattern of melts in equilibrium with younger rdm, older rdm,

713 and rle zircons. Calculated using the zircon-melt REE partition coefficients from Sano et al. (2002).

714 Shown for comparison are the LdM whole rock data (Andersen et al. 2017). Chondrite REE values

715 are from McDonough and Sun (1995).

References

Andersen NL, Singer BS, Coble MA (2019) Repeated Rhyolite Eruption From Heterogeneous Hot Zones Embedded Within a Cool, Shallow Magma Reservoir. JGR SE 124(3):2582-2600 doi:10.1029/2018jb016418

Andersen NL, Singer BS, Costa F, Fournelle J, Herrin JS, Fabbro GN (2018) Petrochronologic perspective on rhyolite volcano unrest at Laguna del Maule, Chile. EPSL 493:57-70 doi:10.1016/j.epsl.2018.03.043

Andersen NL, Singer BS, Jicha BR, Beard BL, Johnson CM, Licciardi JM (2017) Pleistocene to Holocene Growth of a Large Upper Crustal Rhyolitic Magma Reservoir beneath the Active Laguna del Maule Volcanic Field, Central Chile. J Petrol 58(1):85-114 doi:10.1093/petrology/egx006

Bachmann O, Bergantz GW (2004) On the origin of crystal-poor rhyolites: extracted from batholithic crystal mushes. J Petrol 45(8):1565-1582

Bachmann O, Bergantz GW (2006) Gas percolation in upper-crustal silicic crystal mushes as a mechanism for upward heat advection and rejuvenation of near-solidus magma bodies. J Volcanol Geoth Res 149(1-2):85-102

Bai T, Thurber C, Lanza F, Singer BS, Bennington N, Keranen K, Cardona C (2020) Teleseismic tomography of the Laguna del Maule volcanic field in Chile. Journal of Geophysical Research: Solid Earth 125(8):e2020JB019449

Barboni M, Boehnke P, Schmitt AK, Harrison TM, Shane P, Bouvier AS, Baumgartner L (2016) Warm storage for arc magmas. PNAS 113(49):13959-13964 doi:10.1073/pnas.1616129113

Barker S, Wilson C, Smith EG, Charlier B, Wooden JL, Hiess J, Ireland T (2014) Post-supereruption magmatic reconstruction of Taupo volcano (New Zealand), as reflected in zircon ages and trace elements. J Petrol 55(8):1511-1533

Barth AP, Wooden JL (2010) Coupled elemental and isotopic analyses of polygenetic zircons from granitic rocks by ion microprobe, with implications for melt evolution and the sources of granitic magmas. Chem Geol 277(1-2):149-159

Bindeman IN, Fu B, Kita NT, Valley JW (2008) Origin and evolution of silicic magmatism at Yellowstone based on ion microprobe analysis of isotopically zoned zircons. J Petrol 49(1):163-193

Bindeman IN, Simakin AG (2014) Rhyolites—Hard to produce, but easy to recycle and sequester: Integrating microgeochemical observations and numerical models. Geosphere 10(5):930-957

750   Blum TB, Kitajima K, Kita N, Valley JW (2023) Analysis of trace elements in zircon at high mass
751   resolving power using forward-geometry secondary ion mass spectrometry. In: Goldschmidt
752   2023 Conference, vol. GOLDSCHMIDT,

753   Blundy J, Cashman K (2005) Rapid decompression-driven crystallization recorded by melt
754   inclusions from Mount St. Helens volcano. Geology 33(10):793-796

755   Blundy J, Cashman K (2008) Petrologic reconstruction of magmatic system variables and
756   processes. RiMG 69(1):179-239

757   Bodnar R, Student JJ (2006) Melt inclusions in plutonic rocks: Petrography and
758   microthermometry.

759   Boehnke P, Watson EB, Trail D, Harrison TM, Schmitt AK (2013) Zircon saturation re-revisited.
760   Chem Geol 351:324-334

761   Bouvier A-S, Ushikubo T, Kita NT, Cavosie AJ, Kozdon R, Valley JW (2012) Li isotopes and trace
762   elements as a petrogenetic tracer in zircon: insights from Archean TTGs and sanukitoids.
763   Contrib Mineral Petr 163:745-768

764   Bucholz CE, Jagoutz O, VanTongeren JA, Setera J, Wang Z (2017) Oxygen isotope trajectories of
765   crystallizing melts: insights from modeling and the plutonic record. GCA 207:154-184

766   Cashman KV, Sparks RSJ, Blundy JD (2017) Vertically extensive and unstable magmatic systems:
767   a unified view of igneous processes. Science 355(6331):eaag3055

768   Chamberlain KJ, Wilson CJN, Wooden JL, Charlier BLA, Ireland TR (2014) New Perspectives on
769   the Bishop Tuff from Zircon Textures, Ages and Trace Elements. J Petrol 55(2):395-426
770   doi:10.1093/petrology/egt072

771   Charlier B, Wilson C (2010) Chronology and evolution of caldera-forming and post-caldera
772   magma systems at Okataina Volcano, New Zealand from zircon U–Th model-age spectra. J
773   Petrol 51(5):1121-1141

774   Cheng H, Edwards RL, Shen C-C, Polyak VJ, Asmerom Y, Woodhead J, Hellstrom J, Wang Y, Kong
775   X, Spötl C (2013) Improvements in 230Th dating, 230Th and 234U half-life values, and U–Th
776   isotopic measurements by multi-collector inductively coupled plasma mass spectrometry. EPSL
777   371:82-91

778   Claiborne LL, Miller CF, Flanagan DM, Clynne MA, Wooden JL (2010) Zircon reveals protracted
779   magma storage and recycling beneath Mount St. Helens. Geology 38(11):1011-1014

780   Coble MA, Vazquez JA, Barth AP, Wooden J, Burns D, Kylander‐Clark A, Jackson S, Vennari CE
781   (2018) Trace element characterisation of MAD‐559 zircon reference material for ion
782   microprobe analysis. Geostand Geoanal Res 42(4):481-497

783   Contreras C, Cashman KV, Rust A, Cortés M (2022) The influence of magma storage and ascent
784   conditions on Laguna del Maule rhyolite eruptions. J Petrol 63(12):egac121

785   Cooper KM, Kent AJR (2014) Rapid remobilization of magmatic crystals kept in cold storage (vol
786   506, pg 480, 2014). Nature 508(7497):554-554 doi:10.1038/nature13280

787   Cordell D, Unsworth MJ, Diaz D (2018) Imaging the Laguna del Maule Volcanic Field, central
788   Chile using magnetotellurics: Evidence for crustal melt regions laterally-offset from surface
789   vents and lava flows. EPSL 488:168-180 doi:10.1016/j.epsl.2018.01.007

790   Cordell D, Unsworth MJ, Diaz D, Reyes-Wagner V, Currie CA, Hicks SP (2019) Fluid and Melt
791   Pathways in the Central Chilean Subduction Zone Near the 2010 Maule Earthquake (35-36
792   degrees S) as Inferred From Magnetotelluric Data. G3 20(4):1818-1835
793   doi:10.1029/2018gc008167

794   Crowley JL, Schoene B, Bowring S (2007) U-Pb dating of zircon in the Bishop Tuff at the
795   millennial scale. Geology 35(12):1123-1126

796   Danyushevsky LV, Sokolov S, Falloon TJ (2002) Melt inclusions in olivine phenocrysts: using
797   diffusive re-equilibration to determine the cooling history of a crystal, with implications for the
798   origin of olivine-phyric volcanic rocks. J Petrol 43(9):1651-1671

799   Donovan JJ, Singer JW, Armstrong JT (2016) A new EPMA method for fast trace element analysis
800   in simple matrices. Am Mineral 101(8):1839-1853

801   Eiler JM, Crawford A, Elliott T, Farley KA, Valley JW, Stolper EM (2000) Oxygen isotope
802   geochemistry of oceanic-arc lavas. J Petrol 41(2):229-256

803   Feigl KL, Le Mével H, Tabrez Ali S, Córdova L, Andersen NL, DeMets C, Singer BS (2014) Rapid
804   uplift in Laguna del Maule volcanic field of the Andean Southern Volcanic zone (Chile) 2007–
805   2012. Geophysical Journal International 196(2):885-901

806   Ferry JM, Watson EB (2007) New thermodynamic models and revised calibrations for the Ti-in-
807   zircon and Zr-in-rutile thermometers. Contrib Mineral Petr 154(4):429-437 doi:10.1007/s00410-
808   007-0201-0

809   Fierstein J (2018) Postglacial eruptive history established by mapping and tephra stratigraphy
810   provides perspectives on magmatic system beneath Laguna del Maule, Chile. In: AGU Chapman
811   Conference, Integrating Geophysical, Petrochronologic, and Modeling Perspectives on Large
812   Silicic Magma Systems, Quinamavida, Chile January, vol., pp 7-12

813   Ghiorso MS, Evans BW (2008) Thermodynamics of rhombohedral oxide solid solutions and a
814   revision of the Fe-Ti two-oxide geothermometer and oxygen-barometer. Am J Sci 308(9):957-
815   1039

816   Ghiorso MS, Gualda GA (2015) An H_2O–CO_2 mixed fluid saturation model compatible with
817   rhyolite-MELTS. Contrib Mineral Petr 169:1-30

818   Grimes CB, Ushikubo T, John BE, Valley JW (2011) Uniformly mantle-like δ 18 O in zircons from
819   oceanic plagiogranites and gabbros. Contrib Mineral Petr 161:13-33

820   Grimes CB, Wooden JL, Cheadle MJ, John BE (2015) "Fingerprinting" tectono-magmatic
821   provenance using trace elements in igneous zircon. Contrib Mineral Petr 170(5-6) doi:ARTN 46
822   10.1007/s00410-015-1199-3

823   Hildreth W (2004) Volcanological perspectives on Long Valley, Mammoth Mountain, and Mono
824   Craters: several contiguous but discrete systems. J Volcanol Geoth Res 136(3-4):169-198
825   doi:10.1016/j.jvolgeores.2004.05.019

826   Hildreth W, Godoy E, Fierstein J, Singer B (2010) Laguna del Maule volcanic field: Eruptive
827   history of a Quaternary basalt-to-rhyolite distributed volcanic field on the Andean rangecrest in
828   central Chile. In, vol. Servicio Nacional de Geología y Minería,

829   Huber C, Parmigiani A (2018) A physical model for three‐phase compaction in silicic magma
830   reservoirs. Journal of Geophysical Research: Solid Earth 123(4):2685-2705

831   Huber C, Townsend M, Degruyter W, Bachmann O (2019) Optimal depth of subvolcanic magma
832   chamber growth controlled by volatiles and crust rheology. Nat Geosci 12(9):762-+
833   doi:10.1038/s41561-019-0415-6

834   Iacovino K, Matthews S, Wieser PE, Moore G, Bégué F (2021) VESIcal Part I: An open‐source
835   thermodynamic model engine for mixed volatile (H2O‐CO2) solubility in silicate melts. Earth
836   and Space Science 8(11):e2020EA001584

837   Ireland TR, Williams IS (2003) Considerations in zircon geochronology by SIMS. RiMG 53(1):215-
838   241

839   Jaffey A, Flynn K, Glendenin L, Bentley Wt, Essling A (1971) Precision measurement of half-lives
840   and specific activities of U 235 and U 238. Physical review C 4(5):1889

841   Jochum KP, Stoll B, Herwig K, Willbold M, Hofmann AW, Amini M, Aarburg S, Abouchami W,
842   Hellebrand E, Mocek B (2006) MPI‐DING reference glasses for in situ microanalysis: New
843   reference values for element concentrations and isotope ratios. G3 7(2)

844   Kelly JL, Fu B, Kita NT, Valley JW (2007) Optically continuous silcrete quartz cements of the St.
845   Peter Sandstone: High precision oxygen isotope analysis by ion microprobe. GCA 71(15):3812-
846   3832

847   Kita NT, Ushikubo T, Fu B, Valley JW (2009) High precision SIMS oxygen isotope analysis and the
848   effect of sample topography. Chem Geol 264(1-4):43-57

849   Kitajima K, Ushikubo T, Kita NT, Maruyama S, Valley JW (2012) Relative retention of trace
850   element and oxygen isotope ratios in zircon from Archean rhyolite, Panorama Formation, North
851   Pole Dome, Pilbara Craton, Western Australia. Chem Geol 332:102-115

852   Klug JD, Singer BS, Kita NT, Spicuzza MJ (2020) Storage and Evolution of Laguna del Maule
853   Rhyolites: Insight From Volatile and Trace Element Contents in Melt Inclusions. JGR SE 125(8)
854   doi:ARTN e2020JB019475
855   10.1029/2020JB019475

856   Kress VC, Ghiorso MS (2004) Thermodynamic modeling of post-entrapment crystallization in
857   igneous phases. J Volcanol Geoth Res 137(4):247-260

858   Lackey JS, Valley JW, Chen JH, Stockli DF (2008) Dynamic magma systems, crustal recycling, and
859   alteration in the central Sierra Nevada batholith: The oxygen isotope record. J Petrol
860   49(7):1397-1426

861   Le Mével H, Córdova L, Cardona C, Feigl K (2021) Unrest at the Laguna del Maule volcanic field
862   2005–2020: Renewed acceleration of deformation. Bulletin of Volcanology 83(6):39

863   Le Mevel H, Feigl KL, Cordova L, DeMets C, Lundgren P (2015) Evolution of unrest at Laguna del
864   Maule volcanic field (Chile) from InSAR and GPS measurements, 2003 to 2014. Geophys Res Lett
865   42(16):6590-6598 doi:10.1002/2015gl064665

866   Le Mevel H, Gregg PM, Feigl KL (2016) Magma injection into a long-lived reservoir to explain
867   geodetically measured uplift: Application to the 2007-2014 unrest episode at Laguna del Maule
868   volcanic field, Chile. JGR SE 121(8):6092-6108 doi:10.1002/2016jb013066

869   Ludwig K (2001) Squid (1.13 b). A user's manual: Berkeley Geochronology Center Special
870   Publication 2

871   Ludwig KR (2003) Isoplot (3.41d), a geochronological toolkit for Excel. A user's manual: Berkeley
872   Geochronology Center Special Publication 4

873   Mahood G (1990) Second reply to comment of RSJ Sparks, HE Huppert and CJN Wilson
874   on'Evidence for long residence times of rhyolitic magma in the Long Valley magmatic system:
875   the isotopic record in the precaldera lavas of Glass Mountain'. EPSL 99(4):395-399

876   McDonough WF, Sun S-S (1995) The composition of the Earth. Chem Geol 120(3-4):223-253

877   Miller CA, Williams-Jones G, Fournier D, Witter J (2017) 3D gravity inversion and
878   thermodynamic modelling reveal properties of shallow silicic magma reservoir beneath Laguna
879   del Maule, Chile. EPSL 459:14-27

880   Morgan GB, London D (2005) Effect of current density on the electron microprobe analysis of
881   alkali aluminosilicate glasses. Am Mineral 90(7):1131-1138

882   Nasdala L, Corfu F, Schoene B, Tapster SR, Wall CJ, Schmitz MD, Ovtcharova M, Schaltegger U,
883   Kennedy AK, Kronz A (2018) GZ 7 and GZ 8–Two Zircon Reference Materials for SIMS U–Pb
884   Geochronology. Geostand Geoanal Res 42(4):431-457

885   Newman S, Epstein S, Stolper E (1988) Water, carbon dioxide, and hydrogen isotopes in glasses
886   from the ca. 1340 AD eruption of the Mono Craters, California: Constraints on degassing
887   phenomena and initial volatile content. J Volcanol Geoth Res 35(1-2):75-96

888   Newman S, Stolper EM, Epstein S (1986) Measurement of water in rhyolitic glasses; calibration
889   of an infrared spectroscopic technique. Am Mineral 71(11-12):1527-1541

890   Page FZ, Fu B, Kita NT, Fournelle J, Spicuzza MJ, Schulze DJ, Viljoen F, Basei MA, Valley JW
891   (2007) Zircons from kimberlite: new insights from oxygen isotopes, trace elements, and Ti in
892   zircon thermometry. GCA 71(15):3887-3903

893   Pearce NJ, Perkins WT, Westgate JA, Gorton MP, Jackson SE, Neal CR, Chenery SP (1997) A
894   compilation of new and published major and trace element data for NIST SRM 610 and NIST
895   SRM 612 glass reference materials. Geostandards newsletter 21(1):115-144

896   Peres P, Kita NT, Valley JW, Fernandes F, Schuhmacher M (2013) New sample holder geometry
897   for high precision isotope analyses. Surface and Interface Analysis 45(1):553-556

898   Qin Z, Lu F, Anderson AT (1992) Diffusive reequilibration of melt and fluid inclusions. Am
899   Mineral 77(5-6):565-576

900   Reid MR, Vazquez JA (2017) Fitful and protracted magma assembly leading to a giant eruption,
901   Youngest Toba Tuff, Indonesia. G3 18(1):156-177

902   Reid MR, Vazquez JA, Schmitt AK (2011) Zircon-scale insights into the history of a Supervolcano,
903   Bishop Tuff, Long Valley, California, with implications for the Ti-in-zircon geothermometer (vol
904   161, pg 293, 2011). Contrib Mineral Petr 161(2):313-314 doi:10.1007/s00410-010-0564-5

905   Roedder E (1984) Volume 12: fluid inclusions. Reviews in mineralogy 12:644

906   Rose-Koga E, Bouvier A-S, Gaetani G, Wallace P, Allison C, Andrys J, De La Torre CA, Barth A,
907   Bodnar R, Gartner AB (2021) Silicate melt inclusions in the new millennium: a review of
908   recommended practices for preparation, analysis, and data presentation. Chem Geol
909   570:120145

910   Rubin AE, Cooper KM, Till CB, Kent AJ, Costa F, Bose M, Gravley D, Deering C, Cole J (2017)
911   Rapid cooling and cold storage in a silicic magma reservoir recorded in individual crystals.
912   Science 356(6343):1154-1156

913   Sano Y, Terada K, Fukuoka T (2002) High mass resolution ion microprobe analysis of rare earth
914   elements in silicate glass, apatite and zircon: lack of matrix dependency. Chem Geol 184(3-
915   4):217-230

916   Schaen AJ, Schoene B, Dufek J, Singer BS, Eddy MP, Jicha BR, Cottle JM (2021) Transient rhyolite
917   melt extraction to produce a shallow granitic pluton. Sci Adv 7(21):eabf0604

918   Schaen AJ, Singer BS, Cottle JM, Garibaldi N, Schoene B, Satkoski AM, Fournelle J (2018)
919   Textural and mineralogical record of low-pressure melt extraction and silicic cumulate
920   formation in the late Miocene Risco Bayo–Huemul plutonic complex, southern Andes. J Petrol
921   59(10):1991-2016

922   Singer BS, Andersen NL, Le Mével H, Feigl KL, DeMets C, Tikoff B, Thurber CH, Jicha BR, Cardona
923   C, Córdova L (2014a) Dynamics of a large, restless, rhyolitic magma system at Laguna del Maule,
924   southern Andes, Chile. GSA today 24(12):4-10

925   Singer BS, Hildreth W, Vincze Y (2000) 40Ar/39Ar evidence for early deglaciation of the central
926   Chilean Andes. Geophys Res Lett 27(11):1663-1666

927   Singer BS, Jicha BR, Fournelle JH, Beard BL, Johnson CM, Smith KE, Greene SE, Kita NT, Valley
928   JW, Spicuzza MJ (2014b) Lying in wait: deep and shallow evolution of dacite beneath Volcán de
929   Santa María, Guatemala. Geological Society, London, Special Publications 385(1):209-234

930   Singer BS, Le Mével H, Licciardi JM, Córdova L, Tikoff B, Garibaldi N, Andersen NL, Diefenbach
931   AK, Feigl KL (2018) Geomorphic expression of rapid Holocene silicic magma reservoir growth
932   beneath Laguna del Maule, Chile. Sci Adv 4(6):eaat1513

933   Sobolev V, Kostyuk V (1975) Magmatic crystallization based on a study of melt inclusions. Fluid
934   inclusion research 9:182-253

935   Steiger RH, Jäger E (1977) Subcommission on geochronology: convention on the use of decay
936   constants in geo-and cosmochronology. EPSL 36(3):359-362

937   Stelten ME, Cooper KM (2012) Constraints on the nature of the subvolcanic reservoir at South
938   Sister volcano, Oregon from U-series dating combined with sub-crystal trace-element analysis
939   of plagioclase and zircon. EPSL 313:1-11

940   Szymanowski D, Wotzlaw JF, Ellis BS, Bachmann O, Guillong M, von Quadt A (2017) Protracted
941   near-solidus storage and pre-eruptive rejuvenation of large magma reservoirs. Nat Geosci
942   10(10):777-+ doi:10.1038/Ngeo3020

943   Thomas J, Bodnar R, Shimizu N, Chesner C (2003) Melt inclusions in zircon. RiMG 53(1):63-87

944   Valley JW, Kita NT (2009) In situ oxygen isotope geochemistry by ion microprobe. MAC short
945   course: secondary ion mass spectrometry in the earth sciences 41:19-63

946   Valley JW, Lackey JS, Cavosie AJ, Clechenko CC, Spicuzza MJ, Basei MAS, Bindeman IN, Ferreira
947   VP, Sial AN, King EM (2005) 4.4 billion years of crustal maturation: oxygen isotope ratios of
948   magmatic zircon. Contrib Mineral Petr 150(6):561-580

949   Wallace PJ (2005) Volatiles in subduction zone magmas: concentrations and fluxes based on
950   melt inclusion and volcanic gas data. J Volcanol Geoth Res 140(1-3):217-240

951   Wallace PJ, Anderson AT, Davis AM (1999) Gradients in H2O, CO2, and exsolved gas in a large-
952   volume silicic magma system: Interpreting the record preserved in melt inclusions from the
953   Bishop Tuff. JGR SE 104(B9):20097-20122 doi:Doi 10.1029/1999jb900207

954   Wang X-L, Coble MA, Valley JW, Shu X-J, Kitajima K, Spicuzza MJ, Sun T (2014) Influence of
955   radiation damage on Late Jurassic zircon from southern China: Evidence from in situ
956   measurements of oxygen isotopes, laser Raman, U–Pb ages, and trace elements. Chem Geol
957   389:122-136

958   Watson EB, Harrison TM (1983) Zircon saturation revisited: temperature and composition
959   effects in a variety of crustal magma types. EPSL 64(2):295-304

960   Wespestad CE, Thurber CH, Andersen NL, Singer BS, Cardona C, Zeng XF, Bennington NL,
961   Keranen K, Peterson DE, Cordell D, Unsworth M, Miller C, Williams-Jones G (2019) Magma
962   Reservoir Below Laguna del Maule Volcanic Field, Chile, Imaged With Surface-Wave
963   Tomography. JGR SE 124(3):2858-2872 doi:10.1029/2018jb016485

964   Wiedenbeck M, Hanchar JM, Peck WH, Sylvester P, Valley JW, Whitehouse MJ, Kronz A,
965   Morishita Y, Nasdala L, Fiebig J (2004) Further characterisation of the 91500 zircon crystal.
966   Geostand Geoanal Res 28(1):9-39

967   Williams IS (1997) U-Th-Pb geochronology by ion microprobe.

968   Wilson CJN, Charlier BLA (2009) Rapid Rates of Magma Generation at Contemporaneous
969   Magma Systems, Taupo Volcano, New Zealand: Insights from U-Th Model-age Spectra in
970   Zircons. J Petrol 50(5):875-907 doi:10.1093/petrology/egp023

971   Wolff JA, Ellis B, Ramos FC, Starkel WA, Boroughs S, Olin PH, Bachmann O (2015) Remelting of
972   cumulates as a process for producing chemical zoning in silicic tuffs: A comparison of cool, wet
973   and hot, dry rhyolitic magma systems. Lithos 236:275-286

974   Wotzlaw JF, Bindeman IN, Stern RA, D'Abzac FX, Schaltegger U (2015) Rapid heterogeneous
975   assembly of multiple magma reservoirs prior to Yellowstone supereruptions. Sci Rep-Uk
976   5:srep14026
977